Digital Comprehensive Summaries of Uppsala Dissertations
from the Faculty of Science and Technology 2500

Enhancing Hydrodynamic Interaction in Hybrid Wind–Wave Energy Systems

Integrative Methods for Passive Motion Control, Geometry Optimization, and Annual Energy Yield

CHISOM EKWEOBA

ACTA UNIVERSITATIS
UPSALIENSIS
2025

ISSN 1651-6214
ISBN 978-91-513-2377-0
urn:nbn:se:uu:diva-548487

UPPSALA
UNIVERSITET

Dissertation presented at Uppsala University to be publicly examined in 101195, Heinz-Otto Kreiss, Ångströmlaboratoriet, Uppsala, Friday, 14 March 2025 at 08:00 for the degree of Doctor of Philosophy. The examination will be conducted in English. Faculty examiner: Retired Research Fellow Matt Folley (Applied Renewables Research Ltd).

Abstract
Ekweoba, C. 2025. Enhancing Hydrodynamic Interaction in Hybrid Wind–Wave Energy Systems. Integrative Methods for Passive Motion Control, Geometry Optimization, and Annual Energy Yield. *Digital Comprehensive Summaries of Uppsala Dissertations from the Faculty of Science and Technology* 2500. 80 pp. Uppsala: Acta Universitatis Upsaliensis. ISBN 978-91-513-2377-0.

This thesis contains interrelated studies aimed at increasing annual energy produc-tion and enhancing the hydrodynamic interaction within hybrid wind–wave energy converter systems. The first stage investigates how the mass distribution and posi-tion of a wave absorber can be adjusted to enable passive motion control, thereby improving wave energy capture. Following this, a geometric optimization framework is developed for a semi-submersible platform, employing genetic algorithm to identify design parameters that maximize power generation by optimizing the relative motion between the platform and integrated wave absorbers. The research further emphasizes the importance of reliable wave absorber models, demonstrating how robust forecast-ing, using machine learning, methods can be applied to adapt the system for varied oceanic conditions. The study extends the optimization framework to a multi-source offshore renewable energy park that includes wind turbines, floating photovoltaics, and wave converters. A permutation-based aggregator logic, inspired by a 3–8 line decoder and optimized using a genetic algorithm, allows for partial or full curtailment of individual energy sources in discrete steps. This strategy minimizes energy losses at the point of common coupling and balances the capacity factor. Finally, the study examines the impact of the wind turbine's aerodynamic forces on the performance of the wave absorbers, revealing that steady wind conditions enhance wave energy capture, while turbulent wind introduces variability in absorber motion, slightly re-ducing efficiency. Collectively, the findings show an integrated approach, combining analytical models, numerical simulations, and advanced optimization techniques, that can substantially improve wave energy extraction, system stability, and overall annual energy yield.

Keywords: Ballast optimization, pitching wave energy converter, floating platform, geometry optimization, genetic algorithm, machine learning, multi-source renewable integration, permutation-based aggregator, energy loss minimization, capacity factor balancing, hydrodynamic interactions, aerodynamics, hybrid offshore energy systems, wind-wave energy systems

Chisom Ekweoba, Department of Electrical Engineering, Electricity, Box 65, Uppsala University, SE-751 03 Uppsala, Sweden.

ISSN 1651-6214
ISBN 978-91-513-2377-0
URN urn:nbn:se:uu:diva-548487 (http://urn.kb.se/resolve?urn=urn:nbn:se:uu:diva-548487)

To Adimchinobi

List of papers

This thesis is based on the following papers, which are referred to in the text by their Roman numerals.

I Temiz, I., **Ekweoba, C.**, Thomas, S., Kramer, M., Savin, A. (2021).
Wave absorber ballast optimization based on the analytical model for a pitching wave energy converter.
Ocean Engineering, 240, 109906.

II **Ekweoba, C.**, Montoya, D.E., Galera, L., Costa, S., Thomas, S., Savin, A., Temiz, I. (2024).
Geometry optimization of a floating platform with an integrated system of wave energy converters using a genetic algorithm.
Renewable Energy, 231, 120869.

III **Ekweoba, C.**, Montoya, D.E., Galera, L., Costa, S., Savin, A., Temiz, I. (2025).
Machine learning techniques for efficient prediction of a wave energy converter relative motion in a coupled wind and wave energy converter system. *Fluids and Structures*, Under review.

IV Rojas-Delgado, B., **Ekweoba, C.**, Lavidas, G., Temiz, I. (2022).
GA-based permutation logic for grid integration of offshore multi-source renewable parks.
Machines, 10(12), 1208.

V **Ekweoba, C.**, Montoya, D.E., Galera, L., Costa, S., Savin, A., Temiz, I. (2025).
Time-domain analysis of aero-hydro interactions on a floating offshore platform with co-located wind turbine and wave energy converters. *Applied Ocean Research*, Under review.

Contents

Abbreviations

Abbreviation	Description
ACS	Absorber coordinate system
AEP	Annual energy production
BCM	Beam center of moment
BEM	Beam element method
BESS	Battery energy storage system
CAD	Computer aided design
CF	Capacity factor
CFD	Computational fluid dynamics
CoB	Center of buoyancy
CoG	Center of gravity
DoF	Degrees of freedom
ERDF	European Regional Development Fund
FAST2AQWA	Modelling tool combining ANSYS AQWA and OpenFAST
FOWT	Floating offshore wind turbines
FPP	Floating Power Plant
GA	Genetic algorithm
LSTM	Long short-term memory
ML	Machine learning
NREL	National Renewable Energy Laboratory
OFPV	Offshore floating photovoltaic
PCS	Platform coordinate system
PCC	Point of common coupling
PSD	Power spectral density PV
Photovoltaic	
PTO	Power take-off
RAO	Response amplitude operator
RoG	Radius of gyration
SPH	Smoothed Particle Hydrodynamics
SS	Sea state(s)
VOF	Volume of fluid
WA	Wave absorber(s)
WEC	Wave energy converter(s)

List of symbols

Table 1: *List of Symbols*

Greek Letters	
α	Rest angle of the wave absorber.
γ	Summation/index notation.
ω	Wave angular frequency.
θ	Pitch angle of wave absorber.
ρ_b	Density of ballast material.
ρ_w	Density of seawater.
$\zeta(\omega)$	Wave elevation in frequency domain.
Latin Letters & Matrices	
$A(\omega)$	Frequency-dependent added mass.
$\mathbf{A}(\omega)$	Frequency-dependent added mass matrix.
$B(\omega)$	Frequency-dependent radiation damping.
$\mathbf{B}(\omega)$	Frequency-dependen radiation damping matrix.
B_{PTO}	PTO damping coefficient.
$\bar{P}_a$	Mean absorbed power in irregular waves.
$\mathbf{C}$	Hydrostatic stiffness matrix.
C_{hyd}	Hydrostatic/buoyancy restoring coefficient.
C_{grav}	Gravitational restoring coefficient.
$f(H_s, T_p)$	Joint probability density function of H_s and T_p.
$F_{\text{exc}}(\omega)$	Frequency-dependent wave excitation force.
$\mathbf{F}_{\text{exc}}(\omega)$	Frequency-dependent wave excitation forces matrix.
$\mathbf{F}_{\text{rad}}(t)$	Radiation force in time domain.
$\mathbf{F}_{\text{hydrostatic}}(t)$	Hydrostatic restoring force in time domain.
$\mathbf{F}_{\text{other}}(t)$	All other external forces in time domain.
g	Gravitational acceleration.
H_s	Significant wave height.
$H_{\theta,\text{PTO}}(\omega)$	Pitch motion transfer function with PTO.
I	Mass moment of inertia about absorber's pivot.
I_{yy}	Moment of inertia about y-axis.
$I_{yy,b}$	Ballast inertia about the pivot axis.
I^*_{yy}	Base absorber inertia without ballast.
$l_{y,b}$	Length of ballast compartment in y direction.
L	Characteristic length scale.
m_a	Mass of the absorber shell.
m_b	Mass of ballast.
$M_{\text{exc}}(t)$	Excitation moment in time domain.
$M_{\text{rad}}(t)$	Radiation-induced moment in time domain.
$M_{\text{hydrostatic}}(t)$	Hydrostatic restoring moment in time domain.
$M_{\text{other}}(t)$	Other moments in time domain.
$\mathbf{M}$	Mass inertia matrix.
M_{tot}	Total mass.
∇	Submerged volume.

(Continues on next page)

List of Symbols (continued)

$P(\omega)$	Mean absorbed power in regular waves.
r_0, $\vec{r}_0$	Position vector offset for pivot/reference.
$S_{\dot{\theta}\dot{\theta}}(\omega)$	Pitch velocity response spectrum.
$S_\zeta(\omega)$	Wave spectrum.
t	Time variable.
T_p	Peak wave period.
V_b	Volume of ballast compartment.
$\vec{x}_g$	Center of gravity vector.
$\vec{x}_b$	Center of buoyancy vector.
$x_{g,b}$, $z_{g,b}$	Coordinates of ballast CoG in x–z plane.
Operators/Functions	
$\mathrm{i} = \sqrt{-1}$	Imaginary unit in frequency-domain expressions.

1. Introduction

1.1 Wave energy converters: background and fundamentals

The growing emphasis on clean and sustainable energy solutions has spurred a significant shift in global energy conversion practices. Among various renewable technologies, wave energy conversion stands out due to its relatively high energy density and minimal environmental impact [24, 20, 58, 13]. Despite this promising potential, the vast reservoir of ocean wave energy remains largely underexploited, primarily because of challenges related to efficiency, survivability, and financial viability. Although a wide range of wave energy converters (WEC) concepts has been patented over the past few decades, only a limited number have progressed toward commercial deployment [46, 6, 17]. Consequently, improving the overall efficiency of WECs remains a pivotal goal for research and development, as enhancing performance and reducing operational costs would make wave energy more competitive relative to other renewable sources.

WECs are generally classified according to several key criteria, including their operating principle, location, orientation relative to incoming waves, and size in relation to the wavelength. Several studies present reviews of the classifications of wave energy converter technologies, such as [62, 43, 20, 49, 63, 30, 54]. Certain studies have also categorized devices based on their power take-off (PTO) mechanisms [17, 43]. Although various schemes exist, the main distinctions commonly highlight these fundamental aspects of device design and deployment [4, 57, 13].

Based on the operating principle, WECs harness wave energy through different mechanisms. One example is the oscillating water column (OWC) [25, 48, 65, 8], which traps a column of air above seawater that oscillates with incoming waves, driving airflow through a turbine. Another category, overtopping devices [14, 44, 7, 15], collects waves in an elevated reservoir and later releases the water to power low-head turbines. Lastly, wave-activated bodies, such as point absorbers [2, 11, 33, 36] and oscillating surge converters [29, 61, 19], convert the vertical or horizontal motion of a floating or submerged device into electrical power.

Relative to location, the choice of deployment site significantly influences WEC design. Onshore devices can be integrated into the shoreline, sometimes built into existing coastal structures. Nearshore devices occupy shallow waters close to land, while offshore devices are installed

in deeper areas where wave energy is typically greater, often employing floating or anchored systems.

With respect to orientation, the orientation of a device relative to the direction of incoming waves is another important classification metric. Attenuators are elongated systems aligned parallel to the wave direction, capturing energy along their length [16, 64]. Terminator devices [55] are placed perpendicular to wave crests, effectively absorbing by blocking incoming wave energy. Point absorbers are usually small, axisymmetric units moored at a single location, drawing energy from waves that approach from various directions.

When classified based on size relative to wavelength, WECs can also be distinguished by how their physical dimensions compare to the characteristic wavelength of the incident waves. Point absorbers, for example, are typically much smaller than the wavelength, allowing them to capture energy efficiently from all wave directions. Larger devices, such as some attenuators and terminators, have dimensions comparable to or even exceeding the dominant wavelengths. In these cases, the design and positioning must account for the wave spectrum to ensure optimal energy extraction and device survivability.

Another classification focuses on the method by which the mechanical motion of waves is converted into electrical power. The choice of PTO strongly affects both efficiency and reliability [17]. In a hydraulic PTO, high-pressure fluid is routed through hydraulic motors to drive an electrical generator. This design can accommodate irregular wave motions and provide some mechanical smoothing but may suffer from leakage and wear over time [40, 35]. In direct-drive PTO, by eliminating gearboxes and directly coupling wave-induced motion to an electrical generator (e.g., a linear generator [18, 1, 37]), direct-drive systems reduce mechanical losses. However, they typically require specialized materials and more complex designs [1]. Pneumatic PTO is sometimes used [50]. Though relatively robust and mechanically simple, pneumatic systems must handle cyclic airflow patterns and avoid turbine stall under varied sea states.

In addition to hardware design, control strategies are crucial distinctions in WEC. Approaches such as latching or reactive control adjust the PTO damping or phase to synchronize the device's motion with incoming waves. Recent advancements in real-time control leverage wave prediction and sophisticated algorithms to maintain near-optimal performance [51].

However, numerous configurations either partially overlap with these groupings or represent entirely new concepts with different design principles. Regardless of device classification, effective wave-structure interaction modeling is crucial. Hence, comprehensive hydromechanical

analysis and optimization techniques are required to ensure reliable and efficient energy absorption across various sea states [23].

1.1.1 Wave generation mechanisms

The amplitude, frequency, and directionality of waves vary greatly across different regions of the world's oceans, impacting the feasibility and design of wave energy converters [9]. Ocean surface waves are formed due to wind-induced pressure fluctuations and shear stresses at the air-sea interface [41]. Wind speed, fetch, and duration collectively influence the energy transferred to the water column. Additional generation mechanisms include:

- Gravitational forces: Tidal effects modulate wave activity in certain coastal regions, interacting with existing wave fields [24].
- Geological events: Tsunamis triggered by undersea earthquakes or landslides, though sporadic, carry vast amounts of energy.

1.1.2 Wave climate and spectral analysis

Characterizing the wave resource involves long-term statistical data.

- Significant wave height (H_s) and peak period (T_p) are standard parameters for site assessment [13, 53].
- Wave spectra, such as the Pierson–Moskowitz or JONSWAP forms, describe the distribution of energy over frequencies and directions [20].
- Directional spreading functions capture how wave energy is distributed across various heading angles, important for multi-directional seas [3, 10].

These data produce wave scatter diagrams, aiding developers in choosing and designing WECs for a given wave climate [42].

1.1.3 Linear (Airy) wave theory

Linear wave theory assumes small wave steepness and irrotational flow [26, 28]. Despite simplifications, it gives valuable insights into surface elevation and kinematics, dispersion relationship and energy flux.

1.1.4 Higher-order wave theories

When waves are steeper or higher, linear assumptions fail. Stokes' theory and cnoidal wave theory can capture nonlinear effects, like sharper crests or non-sinusoidal profiles. More accurate nonlinear wave theory can

strongly impact predicted loads and performance of WECs in shallow or transitional depth zones [3, 31].

1.1.5 Wave-structure interaction

WECs experience incident-wave forces (diffraction, Froude–Krylov) and radiation forces from device motion [24, 34, 28]. Added mass and damping terms capture fluid inertia and energy dissipation [42]. These terms dictate how effectively a device can resonate or tune to wave conditions [27, 20].

1.1.6 Frequency-domain analysis

Accurate modeling of WECs in real seas needs math formulations plus specialized numerical methods [5]. These capture fluid-structure interactions driving device motion and energy absorptions [32]. For small-amplitude motion, frequency-domain methods linearize wave-structure dynamics [24, 42]. Tools like WAMIT, ANSYS AQWA solve boundary element models, suited to early-stage design [20].

1.1.7 Time-domain simulation and nonlinear effects

Time-domain modeling captures transient behavior, viscous drag, or wave breaking. Morison-type approaches or advanced free-surface tracking handle large amplitude waves [32]. An example is Volume of Fluid (VOF), a free-surface modeling technique used in computational fluid dynamics to track and locate the free surface (or fluid-fluid interface) [59]. Smoothed Particle Hydrodynamics (SPH), a mesh-free, particle-based method that approximates fluid flow by tracking the motion and interactions of particles [45]. Both are widely employed to capture large-amplitude or highly nonlinear wave behavior in time-domain simulations.

1.1.8 Mooring and Station-Keeping Systems

Offshore WECs typically require mooring systems to maintain their intended position and orientation. The choice of mooring configuration and material greatly influences both the device's dynamic response and overall power absorption [38, 34].

Catenary mooring lines lie partly on the seabed and provide restoring forces as wave-induced motion lifts sections of the chain [53]. In contrast, taut-leg mooring systems use continuously tensioned synthetic lines to minimize the seabed footprint [39].

1.2 Floating Power Plant concept

This section is reproduced from the author's licentiate thesis, Chapter 1.2 [23].

The Floating Power Plant[1] (FPP) device consists of a semi-submersible platform held in place by a turret mooring system that allows the platform to rotate passively to face the incoming waves. The FPP's floating platform hosts a single wind turbine and four-WEC. The wind turbine is located close to the mooring point to minimise the rotation of the platform as a result of the wind. Each WEC comprises a partially submerged pitching wave absorber (WA) and an oil hydraulic power take-off system in a dry "engine room" above the free water surface. Each WA contains ballast tanks in its interior and is partially surrounded by the platform on three sides. These surrounding walls of the WA, known as its chamber, aim to improve the hydrodynamic interaction between the platform and the WA. The power production of the wind turbine ranges from 4 MW to 15 MW, while the four WA integrated into the platform have a combined rating of 1 MW to 4 MW, depending on the wave resource. The image of the device is shown in Figure 1.1.

Figure 1.1. The hybrid wind-wave energy project P80. Reproduced with permissions from [60].

[1] www.floatingpowerplant.com

1.3 Problem statement

Despite the growing interest in wave energy, several challenges persist:

- Complex hydrodynamics: Ocean waves are inherently stochastic and multi-directional, posing significant challenges for accurately modeling wave-structure interactions.
- Structural constraints: WECs must withstand harsh marine environments while remaining cost-effective, necessitating innovative design and structural stability solutions.
- Optimization dilemmas: Designing efficient WECs involves balancing multiple, often conflicting objectives (e.g., power capture, structural integrity, maintenance costs).
- Limited real-sea deployments: Data from large-scale prototypes or commercial deployments are still scarce, leading to uncertainties in performance validation and scaling.

This thesis focuses on improving the hydrodynamic interaction of FPP's WECs by developing computationally efficient methods capable of handling the extended degree-of-freedom (DoF) motion between the WAs and the floating platform. In doing so, it addresses the fundamental challenge of balancing accurate dynamic modeling with the practical need to keep simulation times manageable for large-scale design optimization. Beyond the device-level hydrodynamics, the thesis also extends to a system-level grid integration of WECs, investigating how wave converters, coupled with other renewable sources, can be reliably incorporated into electrical networks to meet performance and stability requirements. By unifying both device-centric and grid-centric perspectives, the work presented resolves a twofold problem: (1) efficiently predicting and tuning the motions of the WEC under varying sea states, and (2) ensuring that the resulting power output can be optimally managed and integrated into a broader offshore renewable energy park.

1.4 Thesis aim and objectives

This thesis builds upon the work previously presented in the author's licentiate thesis [23]. The study presented analytical and numerical methods for systems' feature optimization. The aim of this thesis is to advance the hydromechanical modeling and optimization of wave energy converters for enhanced performance and reliability. To achieve this aim, the following objectives are formulated:

1. Passive control of power absorption using ballast configuration selection: An analytical model for optimal ballast search for a wave energy converter is proposed, providing an efficient tool for performance and hydrodynamic optimization of the wave absorber.

2. Integrate optimization strategies: Multi-parameter optimization of the floating platform of a wave energy converter to increase absorption. A practical method to improve the efficiency of genetic algorithm(GA) optimization for the WEC is introduced.
3. Propose techniques for WEC absorption prediction for the coupled wind-wave energy converter system: Using machine learning to efficiently predict WEC motion and absorption for possible integration into real-time WEC control systems.
4. Propose a permutation logic for efficient grid integration of WEC and other renewable energy sources.
5. Fully coupled aerodynamic–hydrodynamic analysis: Evaluate how different wind conditions, steady or turbulent, affect floating platform dynamics and wave absorber performance in an offshore colocated wind-wave energy converter systems.

1.5 Thesis structure

This thesis is structured to present a comprehensive overview of the research and its findings:

- Chapter 1 – Introduction: Provides the background, fundamentals of wave energy conversion, the Floating Power Plant concept, problem statement, research gap, and the main objectives of the thesis.
- Chapter 2 – Theory: Presents the theory upon which the research studies are based.
- Chapter 3 – Methods: Describes the methods used for hydromechanical modeling, as well as the optimization strategies employed to improve WEC performance.
- Chapter 4 and 5 – Results and Discussion: Integrates the results from the individual papers, discussing how they collectively address the research gap. Highlights challenges, limitations, and the broader implications for wave energy deployment.
- Chapter 6 and 7 – Conclusions and Future Work: Presents the main conclusions of the thesis, offers recommendations for future research.
- Chapter 8 – Summary of included papers: Summarizes the methodologies, key findings, and conclusions of the papers that form the core of this thesis.
- References: Contains all cited sources used in the comprehensive chapters.

2. Theory

This chapter unifies the theoretical foundations presented across the studies constituting this thesis, examining both the core concepts of pitching wave energy converters (WECs) on floating platforms and advanced approaches for machine-learning-based wave-structure interaction predictions. It also addresses control strategies for multi-source renewable power parks. Another study explores the fully coupled aero-hydrodynamics of a floating wind-wave system. Building upon linear frequency-domain models, **Paper I** explains ballast-driven resonance tuning and derives response amplitude operators (RAOs) for pitching WECs. **Paper II** then uses a genetic algorithm to optimize multi-degree-of-freedom platform-WEC geometry, maximizing annual energy output under stability constraints. In parallel, **Paper III** couples high- and low-fidelity models with neural networks, delivering data-driven predictions of wave-structure interactions in the time domain. Next, **Paper IV** develops a permutation-logic aggregator control for offshore renewable parks, employing a genetic algorithm to selectively disconnect devices and reduce energy losses while stabilizing capacity factors. Lastly, **Paper V** extends these studies to a fully-coupled, time-domain analysis of the floating wind turbine, its platform and the integrated pitching WECs.

The goal is to provide a coherent overview of the main concepts and equations underpinning these research efforts.

2.1 Pitching wave energy converters and ballast optimization (Paper I)

2.1.1 Physical description and coordinate system

A pitching WEC typically consists of a partially submerged wave absorber (WA) mounted on a hinge located above the still-water line (Figure 2.1). The hinge axis allows the absorber to rotate about one principal axis (usually the y-axis). The angle between the horizontal plane and the hinge-arm of the absorber is called the *rest angle*, α. When no waves are present, the absorber remains at this rest angle. Ballast compartments, filled with water or other dense matter, are used to shift the center of gravity (CoG) and achieve a desired α.

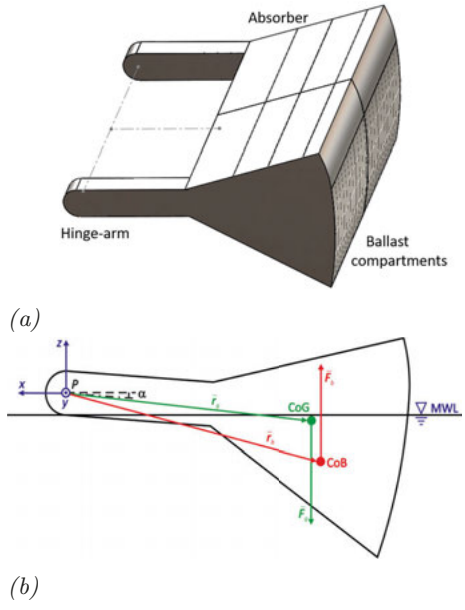

Figure 2.1. Wave absorber geometry with pivot point P above still-water level and rest angle α; (a) CAD representation and (b) side view with main forces. Adapted from [56].

2.1.2 Equation of motion for a pitching absorber

Following Newton's second law, the rotational equation of motion for a pitch-type absorber around the pivot point (the y-axis) can be written as [56]:

$$I\,\ddot{\theta}(t) \;=\; M_{\mathrm{exc}}(t) \;-\; M_{\mathrm{rad}}(t) \;-\; M_{\mathrm{hydrostatic}}(t) \;-\; M_{\mathrm{other}}(t), \qquad (2.1)$$

where

- I is the mass moment of inertia about the pitch axis,
- M_{exc} is the pitch-excitation moment from incident and scattered waves,
- M_{rad} is the radiation-induced pitch moment,
- $M_{\mathrm{hydrostatic}}$ combines buoyancy and gravity restoring,
- M_{other} can include drag, mooring, or power take-off (PTO) forces.

A linear potential-flow assumption allows transformation of (2.1) into the frequency domain; the pitch-response amplitude operator (RAO) in waves of frequency ω is

$$\Theta(\omega) \;=\; \frac{M_{\mathrm{exc}}(\omega)}{-\,\omega^2\big(I + A(\omega)\big) \;+\; j\,\omega\,B(\omega) \;+\; C_{\mathrm{hyd}}}, \qquad (2.2)$$

where $A(\omega)$ and $B(\omega)$ are the pitch added mass and radiation damping, and C_{hyd} is the linear hydrostatic stiffness. The absorber's resonance period depends primarily on I and C_{hyd} [56].

2.1.3 Mass matrix

For a rigid, freely floating body in 6 DOF, the mass matrix $\mathbf{M}$ takes the form

$$\mathbf{M} = \begin{bmatrix} m & 0 & 0 & 0 & mz_g & -my_g \\ 0 & m & 0 & -mz_g & 0 & mx_g \\ 0 & 0 & m & my_g & -mx_g & -mx_g \\ 0 & -mz_g & my_g & I_{xx} & I_{xy} & I_{xz} \\ mz_g & 0 & -mx_g & I_{yx} & I_{yy} & I_{yz} \\ -my_g & mx_g & 0 & I_{zx} & I_{zy} & I_{zz} \end{bmatrix}, \tag{2.3}$$

where $m = \nabla\rho$ denotes the mass of the body, ∇ is the submerged volume, ρ is the density of water, (x_g, y_g, z_g) are coordinates of its center of gravity, and $I_{ij=x,y,z}$ are the moments of inertia.

Center of gravity

In this thesis, the pitch angle of the hinged arm relative to the horizontal is called the rest angle, α, shown in Figure 2.1(b). The rest angle significantly affects hydrodynamics by changing the geometry and volume of the submerged section, the position of the center of gravity and buoyancy, and thereby the interaction of the WA with the surrounding chamber.

If the WA is composed of a steel shell plus several ballast compartments, the total mass M_{tot} is

$$M_{tot} = \sum_{\gamma=1}^{N} m_\gamma, \tag{2.4}$$

where N is the number of components (steel shell plus selected ballast compartments), and m_γ are their respective masses. The total WA center of gravity $\vec{CoG}_{tot}$ depends on individual mass contributions and centers of gravity, $\vec{cog}_\gamma$:

$$\vec{CoG}_{tot} = \frac{\sum_{\gamma=1}^{N} m_\gamma \, \vec{cog}_\gamma}{M_{tot}}. \tag{2.5}$$

Additionally, the mass and center of gravity are linked to the submerged volume ∇ (with water density ρ_w) via

$$M_{tot}\, x_g = \nabla\, \rho_w\, \vec{x}_b, \tag{2.6}$$

where x_g and x_b are the x-coordinates of $\vec{CoG}_{tot}$ and $\vec{CoB}_{tot}$ (center of buoyancy), respectively, assuming symmetry about the xz-plane. Splitting the system into ballast mass m_b and absorber shell mass m_a, we

obtain

$$M_{tot} x_g = m_a x_{g,a} + m_b x_{g,b}, \tag{2.7}$$
$$M_{tot} z_g = m_a z_{g,a} + m_b z_{g,b}, \tag{2.8}$$

which, combined with Eq. (2.6), yields

$$m_b \, \vec{x}_{g,b} = \nabla \, \rho_w \, \vec{x}_b - m_a \, \vec{x}_{g,a}. \tag{2.9}$$

Hence, adjusting ballast location affects both the submerged volume and the rest angle.

Inertia moment
Suppose the WA frame is initially unrotated, and its inertia is I. For a rotation α about the pivot P, the pitch rotation matrix about the y-axis is

$$\mathbf{R}_y(\alpha) = \begin{bmatrix} \cos\alpha & 0 & \sin\alpha \\ 0 & 1 & 0 \\ -\sin\alpha & 0 & \cos\alpha \end{bmatrix}. \tag{2.10}$$

The rotated inertia matrix in the WA frame is

$$\mathbf{I}_R(\theta) = \mathbf{R}_y^{\mathrm{T}} \, I \, \mathbf{R}_y, \tag{2.11}$$

where I is the original (unrotated) moment of inertia. Translating $\mathbf{I}_R$ to the global frame, assuming parallel axes between the WA and global coordinates, requires adding

$$\mathbf{I}_T = \mathbf{I}_R + \mathbf{T}, \tag{2.12}$$

where

$$\mathbf{T} = M_{tot} \begin{bmatrix} y_0^2 + z_0^2 & -x_0 y_0 & -x_0 z_0 \\ -x_0 y_0 & x_0^2 + z_0^2 & -y_0 z_0 \\ -x_0 z_0 & -y_0 z_0 & x_0^2 + y_0^2 \end{bmatrix}, \tag{2.13}$$

and $\vec{r}_0 = (x_0, y_0, z_0)$ is the vector from the global origin to the WA origin. For ballast specifically, if $\vec{r}_{g,b} = (x_{g,b}, 0, z_{g,b})$ denotes the ballast center of gravity, then its I_{yy} in global coordinates becomes

$$I_{yy} = I^*_{yy} + m_b\big(x_{g,b}^2 + z_{g,b}^2\big), \tag{2.14}$$

where I^*_{yy} is the absorber's base moment of inertia.

2.2 Power absorption

The mean power absorbed by a wave absorber (WA) in regular waves can be approximated by [26]:

$$P(\omega) = \tfrac{1}{2} \, B_{pto} \, \omega^2 \, |\Theta|^2, \tag{2.15}$$

where ω is the regular-wave frequency, Θ the displacement amplitude, and B_{pto} the PTO damping coefficient.

For irregular waves, the wave spectrum $S_\zeta(\omega)$ defines the sea state. The corresponding response spectrum of the absorber's angular velocity $\dot{\theta}$ is [47]:

$$S_{\dot{\theta}\dot{\theta}}(\omega) = \left|H_{\dot{\theta},\,pto}(j\omega)\right|^2 S_\zeta(\omega) = \omega^2 \left|H_{\theta,\,pto}(j\omega)\right|^2 S_\zeta(\omega), \tag{2.16}$$

where $\left|H_{\dot{\theta},\,pto}(j\omega)\right|$ is the absorber's angular velocity transfer function including PTO effects. Thus, the mean absorbed power in irregular seas becomes

$$\bar{P}_a = B_{pto} \int_0^\infty S_{\dot{\theta}\dot{\theta}}(\omega)\, d\omega = B_{pto} \int_0^\infty \omega^2 \left|H_{\theta,\,pto}(j\omega)\right|^2 S_\zeta(\omega)\, d\omega. \tag{2.17}$$

2.3 Floating platform geometry optimization and multi-DOF formulation (Paper II)

For a 6-DOF motion, the matrices in the equation of motion, such as $\mathbf{M}$ and $\mathbf{A}$ in Eq. 2.18, are 6×6. In scenarios where additional modes of motion apply (e.g., a hinged part of the submerged body pitching relative to a platform or a deformable body), the system expands to an $N \times N$ form, where $N = 6 + i$ and i is the number of extended DOFs.

2.3.1 Multi-DOF platform + WEC equations of motion

For a floating platform with up to 6 rigid-body DOFs plus additional WEC pitch DOFs, the system can be represented in the frequency domain by:

$$\Big[-\omega^2\big(\mathbf{M} + \mathbf{A}(\omega)\big) \;+\; j\,\omega\,\mathbf{B}(\omega) \;+\; \mathbf{C}\Big]\,\mathbf{X}(\omega) \;=\; \mathbf{F}_{\text{exc}}(\omega), \tag{2.18}$$

where

- $\mathbf{X}(\omega)$ is the vector of complex amplitudes for each DOF (e.g., $6+i$ modes),
- $\mathbf{A}(\omega)$, $\mathbf{B}(\omega)$ are added mass and radiation damping,
- $\mathbf{C}$ is the hydrostatic stiffness (buoyancy + gravity),
- $\mathbf{F}_{\text{exc}}(\omega)$ is the linear wave-excitation force/moment.

2.3.2 Genetic algorithm for geometry optimization

Paper II proposes a GA to optimize the geometry of the floating structure for maximum annual energy production (AEP). The steps are as follows:

1. Initialization: Randomly generate a combination of design candidates (e.g., pontoon spacing, spoiler dimensions).
2. Mass & hydrodynamic coefficients computation: For each combination of candidates, compute the total mass distribution and re-run the potential flow solver (e.g., WAMIT) to get updated $\mathbf{A}(\omega), \mathbf{B}(\omega), \mathbf{C}$.
3. Objective Function: Evaluate AEP and absorption bandwidth. The objective is
$$f_{\text{obj}} = \text{AEP} \times w_n(\text{RAO}), \tag{2.19}$$
where $w_n(\text{RAO})$ is a weighting factor that penalizes overly narrow resonance peaks.
4. Constraints: Static heel and trim angles must not exceed some threshold, ensuring the platform remains stable enough to support a wind turbine.
5. Selection & Reproduction: GA operators (crossover, mutation, elitism) create new candidate geometries for the next generation.
6. Convergence: Continue until the maximum generation is reached or the solution converges.

2.4 Machine-learning based predictions of complex wave-structure interactions (Paper III)

2.4.1 Multi-step LSTM model

The multi-step model treats the absorber pitch prediction as a sequential forecasting task. Let $\{x_t\}$ be the measured platform states and wave conditions, and let $\{y_t\}$ be the target absorber pitch. A Long-short-term memory (LSTM) network takes in a window of past inputs $(x_{t-W+1}, \ldots, x_t)$ and outputs $\hat{y}_{t+\Delta t}$. By advancing a sliding window over the entire time series, the model learns to forecast the short-term future motion repeatedly without using its own predictions as inputs (thus avoiding error accumulation).

The LSTM includes gating mechanisms:

$$f_t = \sigma(W_f[h_{t-1},\, x_t] + b_f), \quad i_t = \sigma(W_i[h_{t-1},\, x_t] + b_i),$$

$$\tilde{C}_t = \tanh(W_c[h_{t-1},\, x_t] + b_c), \quad C_t = f_t \odot C_{t-1} + i_t \odot \tilde{C}_t,$$

$$o_t = \sigma(W_o[h_{t-1},\, x_t] + b_o), \quad h_t = o_t \odot \tanh(C_t).$$

Here, σ is the logistic function, and $\odot$ denotes element-wise multiplication. x_t is the input vector at time step t, h_{t-1} is the hidden state from the previous time step, and W_f, W_i, W_o, W_c are the weight matrices associated with the forget, input, output, and cell state operations,

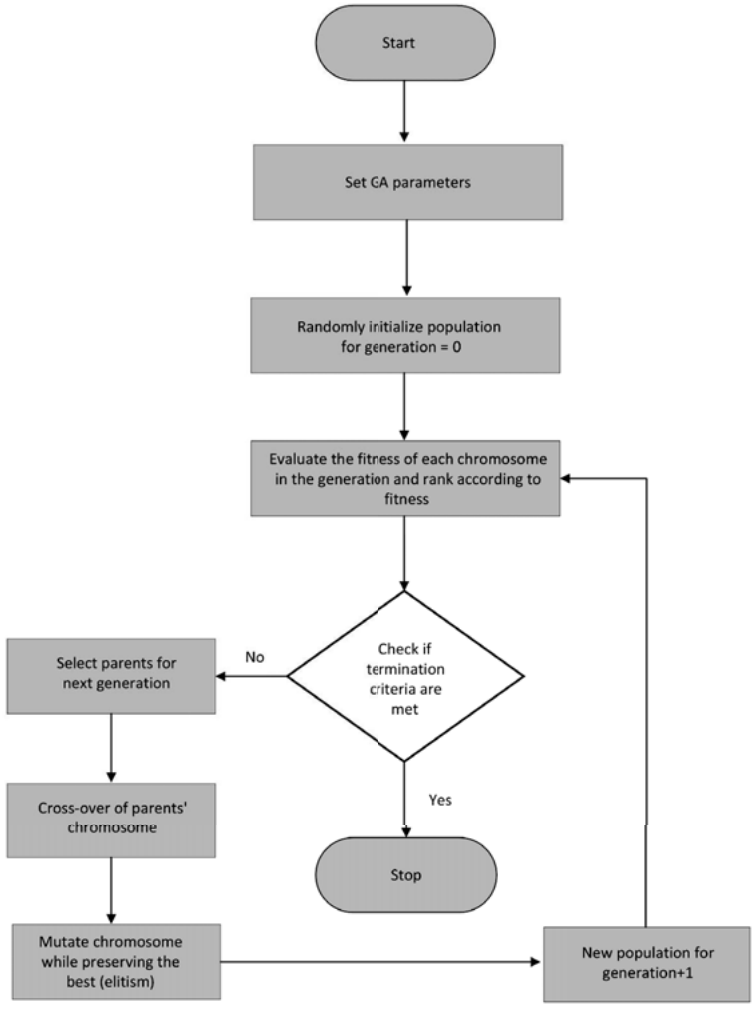

Figure 2.2. Genetic algorithm process flow [21].

respectively. The final hidden state h_t is passed to a dense layer that outputs the absorber relative pitch motion. The training uses the mean squared as the loss function to minimize prediction error:

$$\mathcal{L} = \frac{1}{N} \sum_{i=1}^{N} (y_{i,\text{true}} - y_{i,\text{pred}})^2.$$

An Adam optimizer with early stopping is employed to avoid overfitting. Some important hyperparameters include the LSTM unit count, dropout rate, learning rate, and sequence length W. Hyperparametres are tuned to minimize prediction error. Figure 2.3 shows the LSTM architecture.

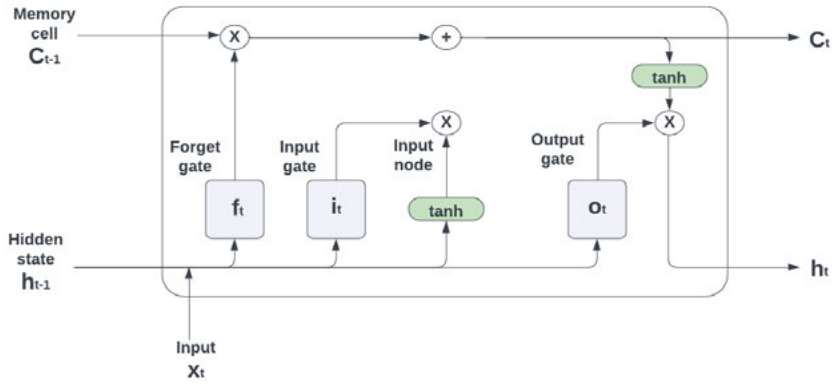

Figure 2.3. LSTM architecture [12].

2.4.2 Hybrid physics–ML model

The hybrid model augments the LSTM inputs with static physics-based features, such as added mass, radiation damping, and mooring stiffness, which are derived from potential-flow analysis and structural data. Let $\mathbf{p}$ denote these physics-based vectors or matrices. By concatenating $\mathbf{p}$ with the time-series inputs, the network learns higher-order phenomena while remaining grounded in physical constraints. Symbolically, the prediction can be expressed as

$$\hat{y}_{t+\Delta t} = f_{\mathrm{ML}}\big(x_t,\, x_{t-1},\, \ldots,\, \mathbf{p}\big).$$

This hybrid approach reduces the data volume needed to capture nonlinear wave-structure interactions and improves generalization across different sea states.

2.5 GA-based permutation logic for multi-source offshore parks (Paper IV)

2.5.1 Problem statement

In **Paper IV**, the focus shifts from a single WEC-floating platform to a larger multi-source renewable park comprising offshore floating PV, wind turbines, and wave converters. The system must be integrated at a point of common coupling, (PCC), to the grid. A major challenge is minimizing energy losses or curtailment while meeting demand constraints.

2.5.2 Key performance indicators

- Energy losses:

$$\text{Losses} \;=\; \int (\text{Supply} - \text{Demand})^{+}\, \mathrm{d}t,$$

- Capacity factor: For combined sources at the aggregator,

$$C_{f,\text{combined}} \;=\; \frac{\sum_{n=1}^{N} E_{\text{out},n}}{\sum_{n=1}^{N} P_{n,\text{rated}} \times T_{\text{int}}}, \tag{2.20}$$

- Seasonal performance: **Paper IV** also looks at how partial curtailments vary across winter vs. summer wave/solar resource distributions.

Such analysis reveals that enabling partial disconnections or permutations can reduce overall energy losses, especially when certain sources produce excess power relative to the local demand or grid constraints.

2.6 Coupled aero-hydrodynamic analysis of floating wind-wave energy systems (Paper V)

2.6.1 Time-domain approach and modeling framework

In **Paper V**, the thesis extends frequency-domain and data-driven methods to a fully coupled, time-domain analysis of the offshore wind turbine, its platform and the integrated pitching WECs. The model relies on two components, ANSYS AQWA, to derive potential-flow hydrodynamic coefficients and NREL's OpenFAST, a blade-element momentum (BEM) code for aerodynamic thrust, torque, and rotor–tower interaction. Apparently, platform motions affect rotor inflow and absorber relative motions, while rotor thrust and absorber PTO torques feed back into the platform's global dynamics.

2.6.2 Aerodynamic loading

Aerodynamic loading on the rotor is computed through a blade-element momentum (BEM) approach within OpenFAST. Each blade is divided into N radial segments. For segment i at radial position r_i, the local inflow angle ϕ_i and the angle of attack α_i are computed based on the relative velocity of airflow around the blade element. If $\theta_{p,i}$ is the local blade pitch angle, then

$$\alpha_i \;=\; \phi_i \;-\; \theta_{p,i}, \tag{2.21}$$

where ϕ_i is found by considering both the axial and tangential components of the incoming wind velocity (including any induced velocity due to rotor operation and potential platform motion).

Local aerodynamic forces.
Once α_i is known, airfoil data are used to retrieve the lift and drag coefficients, $c_\ell(\alpha_i)$ and $c_d(\alpha_i)$. For an element with chord length c_i, width dr_i, and relative wind speed $V_{\text{rel},i}$, the incremental aerodynamic force $d\mathbf{F}_{\text{aero},i}$ can be expressed in the local 2D blade-element frame as:

$$dF_{\ell,i} \;=\; \tfrac{1}{2}\,\rho_{\text{air}}\,c_i\,dr_i\;c_\ell(\alpha_i)\,\big(V_{\text{rel},i}\big)^2 \tag{2.22}$$

$$dF_{d,i} \;=\; \tfrac{1}{2}\,\rho_{\text{air}}\,c_i\,dr_i\;c_d(\alpha_i)\,\big(V_{\text{rel},i}\big)^2, \tag{2.23}$$

where ρ_{air} is the density of air. Typically, $dF_{\ell,i}$ is directed perpendicular to $V_{\text{rel},i}$, and $dF_{d,i}$ is aligned with $V_{\text{rel},i}$. Therefore, the incremental aerodynamic force can be written as:

$$d\mathbf{F}_{\text{aero},i} \;=\; \big(dF_{\ell,i}\big)\,\hat{\mathbf{e}}_\perp \;+\; \big(dF_{d,i}\big)\,\hat{\mathbf{e}}_\parallel, \tag{2.24}$$

where $\hat{\mathbf{e}}_\perp$ and $\hat{\mathbf{e}}_\parallel$ are the unit vectors perpendicular and parallel to the relative wind direction in the local blade section frame.

Thrust and torque.
To get total thrust and torque on the entire rotor, one projects $d\mathbf{F}_{\text{aero},i}$ onto the rotor's axial and tangential directions, then sums over all N blade elements:

$$\mathbf{F}_{\text{aero}} \;=\; \sum_{i=1}^{N} \mathbf{T}_{\text{elem}\to\text{global}}\big(d\mathbf{F}_{\text{aero},i}\big), \tag{2.25}$$

$$Q_{\text{rotor}} \;=\; \sum_{i=1}^{N}\Big[\, r_i\;\hat{\mathbf{e}}_\theta(r_i)\;\cdot\;\mathbf{T}_{\text{elem}\to\text{global}}\big(d\mathbf{F}_{\text{aero},i}\big)\Big], \tag{2.26}$$

where $\mathbf{T}_{\text{elem}\to\text{global}}$ is the appropriate transformation from the local element frame to global or hub coordinates, and r_i is the radial position of the blade element. The net thrust vector $\mathbf{F}_{\text{aero}}$ and rotor torque Q_{rotor} are then passed to the platform's global equations of motion.

Each pitching WEC is modeled as an additional DOF that augments the floating platform's six rigid-body motions as described by equation (2.1). By applying the BEM approach at each timestep, FAST captures how changing wind conditions, blade pitch angles, wave absorber and platform motions interact. This method provides the rotor thrust and torque in the global frame, which is then inserted into the floating system's global equation of motion, offering a comprehensive time-domain

simulation of a wind-wave energy platform under both aerodynamic and hydrodynamic loads.

Collectively, **Papers I–V** provide a unified framework by integrating these insights—ranging from linear hydrodynamics, frequency-domain and time-domain analyses, to advanced data-driven prediction, and finally system-level multi-source GA control—an end-to-end perspective is formed, addressing multiple aspects of wave energy converter design, optimization, and grid integration.

3. Methods

3.1 Optimization approaches (Paper I and Paper II)

3.1.1 Ballast configuration (Paper I)

Paper I presents a procedure for optimizing ballast in a pitching absorber to shift its resonance frequency and rest angle without repeatedly redesigning the geometry in external CAD. The absorber's internal compartments can be filled or left empty to modify the moment of inertia about the pivot and hydrostatic stiffness. A frequency-domain solver (via WAMIT) then provides added mass, radiation damping, and excitation moments for each potential ballast configuration. The approach proceeds as follows:

1. Calculate mass properties of the empty absorber.
2. Select a target rest angle α.
3. Enumerate possible ballast masses and center-of-gravity locations to achieve α.
4. Verify geometric feasibility (compartment constraints,e.g., ensuring ballast compartments fit within the shell).
5. Update moments of inertia, hydrostatic restoring, and hydrodynamic properties.
6. Identify configurations that optimizes the resonance frequency, RAO amplitude, or overall power capture.

A typical equation for ballast mass in each compartment is:

$$m_b = \rho_b V_b, \tag{3.1}$$

where ρ_b is ballast density and V_b is the compartment volume. A minimum feasible cross-section ensures structural viability:

$$A_b \geq A_{\min}, \tag{3.2}$$

with A_b representing the cross-sectional area. The center of gravity (CoG) for a given configuration is found via

$$x_{\mathrm{CoG}} = \frac{\sum_i m_i \, x_i}{\sum_i m_i}, \tag{3.3}$$

and analogous expressions for other coordinates. By systematically evaluating multiple ballast layouts, **Paper I** demonstrates how to tune wave absorber pitch resonance and optimize power absorption across a relevant wave spectrum.

3.1.2 Genetic algorithm for platform geometry (Paper II)

Paper II employs a GA to refine platform geometry for maximizing AEP and broadening the device's operational bandwidth. Variables include pontoon spacing, spoiler geometry. A parametric interface in WAMIT (a FORTRAN subroutine `GEOMXACT.F`) updates panel meshes quickly with each GA iteration.

A beam model, [23], approximates the platform's structural mass distribution by summing individual beam segments with known densities. The wave excitation, radiation, and hydrostatic matrices are then computed via WAMIT, followed by an AEP calculation integrating absorbed power over different sea states. If the platform's static heel or trim angle exceeds 5°, the GA penalizes or sets the design's fitness to zero:

$$f_{\text{obj}} = \begin{cases} 0, & \text{if heel or trim} > 5^\circ, \\ \text{AEP} \times w_n(\text{RAO}), & \text{otherwise.} \end{cases} \tag{3.4}$$

Here, $w_n(\text{RAO})$ is a weighting term tied to average RAO performance over a specified wave-period range, preventing narrow resonance spikes from inflating AEP estimates unrealistically. This yields optimized platform geometries that capture substantial wave energy while meeting the stability criteria. Since the search for an optimum result can quickly become computationally expensive as the number of characteristic features to be optimized increases, the solution space is refined by tactically curtailing the permitted span of the characteristic features. Figure 4.12 how the span is determined using single variable parametric sweep.

3.2 Hybrid physics-based and machine-learning methods (Paper III)

Paper III emphasizes high-fidelity time-domain simulations and data-driven modeling. A workflow like FAST2AQWA incorporates hydrodynamic coefficients (e.g., added mass, radiation damping) from ANSYS AQWA and couples them with aerodynamic/structural modules in OpenFAST to capture intricate floating-platform responses. On top of these physics-based time-series, multi-step and hybrid ML models (using LSTM networks) are trained to predict the relative motion over extended periods. By merging static linear-hydrodynamic matrices with nonlinear corrections learned by ML, **Paper III** reports:

- Improved prediction accuracy for dynamic wave-platform interactions.
- Faster evaluation times than purely high-fidelity simulations.

- Enhanced potential for adaptive control strategies based on real-time forecasts of absorber responses.

These ML-driven methods complement frequency-domain solvers and GA-based geometry/ballast/permutation optimizations by handling complex, transient, or strongly coupled behaviors.

The algorithm for the hybrid physics–ML model is shown in Figure 3.1.

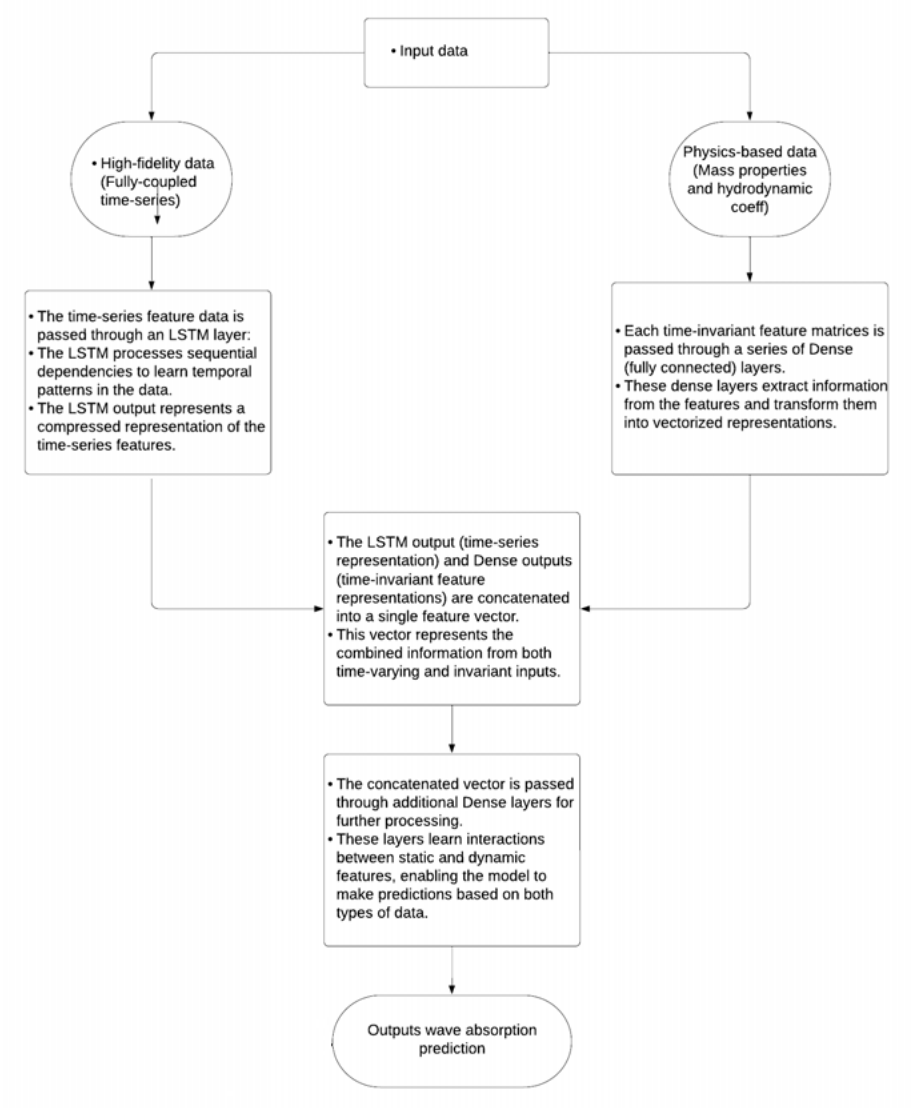

Figure 3.1. Flowchart illustrating the hybrid physics–ML model algorithm for wave energy absorption prediction [12].

3.3 GA-Based permutation logic for multi-source offshore renewable integration (Paper IV)

Paper IV aims at efficiently integrating multiple offshore renewable sources at a common point of coupling to the grid. A GA-based permutation logic is applied to an aggregator that can partially or fully connect each source to reduce energy losses and facilitate demand matching.

3.3.1 Permutation logic and aggregator concept

Instead of standard operational rules (each source always tries to produce its maximum), a permutation logic is proposed, akin to an electronic multiplexer or "3-8 line decoder." Each source can operate at {0, 0.5, 1.0} of its rated power, and a control logic determines which combination (permutation) to use:

1. *Input states:* Real-time data on demand, net energy losses, and possible partial output from each source.
2. *Decoder logic:* Like a digital multiplexer, it chooses how much each source contributes (0, 50%, or 100%).
3. *Feedback:* The aggregator checks if curtailing or enabling certain sources best meets demand or lowers PCC losses.

Mathematically, the aggregator output at time t, Output(t), may be a weighted sum:

$$\text{Output}(t) \;=\; \sum_{n=1}^{N} \mathsf{perc}_n(t) \;\times\; P_n(t), \tag{3.5}$$

where $\mathsf{perc}_n \in \{0, 0.5, 1.0\}$ is the fraction used for source n (wind, wave, or PV), and $P_n(t)$ is that source's instantaneous power.

3.3.2 Genetic algorithm for permutation optimization

Though the aggregator can implement a fixed logic table, **Paper IV** uses a GA to adapt the partial-disconnect logic across the year or under varying demand. The single-objective GA is formulated to minimize total energy losses, subject to constraints on each source's delivered output (e.g., partial curtailment up to some fraction of its available power). When demand exceeds generation, no curtailment is imposed; otherwise, the GA systematically selects which sources to reduce. If more generation still remains after curtailment, the excess can be diverted to a battery energy storage system (BESS) or other loads [52]. Once the GA converges to optimal or near-optimal permutations, the residual gap between pre- and post-curtailment generation can inform the sizing of an offshore or onshore BESS.

3.4 Fully coupled wind-wave interaction (Paper V)

In **Paper V**, the fully coupled aero-hydro analysis is presented. The approach proceeds as follows:

1. Hydrodynamic computation: Before the time-domain simulation, AQWA computes frequency-dependent added mass, radiation damping, and wave-excitation forces for the floating platform geometry (including the attached WECs). These data can then be represented by convolution integrals, capturing radiation-memory effects by convolving past platform velocities with the radiation impulse response functions derived from AQWA's frequency-domain analysis.

   In each timestep, the hydrodynamic forces are updated based on instantaneous platform/WEC motions and the wave input.
2. Aerodynamic load: The wind turbine is modeled with blade-element momentum (BEM) theory (Sec. 2.6.2). At each timestep, OpenFAST solves for the aerodynamic thrust and torque on the rotor blades, accounting for platform motions (e.g., pitch, surge, heave) that modify the effective wind inflow. The turbine's controllers (blade pitch, generator torque) also operate on a timestep-by-timestep basis, adapting rotor behavior to wind conditions.
3. Coupled equations of motion: The instantaneous hydrodynamic and aerodynamic forces are then fed into the global system. The Fast2Aqwa interface ensures the consistent exchange of state variables and the latest hydrodynamic/aerodynamic loads at each timestep.
4. Time-domain outputs and RAO post-processing: After completing the simulation, `Fast2Aqwa` provides time histories of all relevant motions, plus the corresponding wave elevation, as well as aerodymnamic thrusts and torque. To extract frequency-response characteristics, cross-spectral, $S_{x\eta}(\omega)$, and auto-spectral, $S_{\eta\eta}(\omega)$, densities are computed:

$$S_{x\eta}(\omega) = \mathrm{E}\{X(\omega)\,^*(\omega)\}, \quad S_{\eta\eta}(\omega) = \mathrm{E}\{(\omega)\,^*(\omega)\}, \tag{3.6}$$

   where $X(\omega)$ and (ω) are the Fourier transforms of a given platform/WEC motion and the wave elevation, respectively. The RAO is found as follows:

$$\mathrm{RAO}_x(\omega) \;=\; \left|\frac{S_{x\eta}(\omega)}{S_{\eta\eta}(\omega)}\right|. \tag{3.7}$$

   By computing RAOs under different wind conditions, **Paper V** investigates how aerodynamic forces from the wind turbine shift resonance peaks, alter WEC pitch amplitudes, and ultimately impact wave-energy capture performance. Comparisons across these

scenarios highlight the effect of wind state on the integrated wind-wave system's dynamics.

This study combines potential-flow hydrodynamics from AQWA with aerodynamic and structural modeling in OpenFAST, enabling a comprehensive time-domain analysis of the floating wind-wave system. The aim is to evaluate the dynamic interactions between wind turbine thrust and wave energy conversion, providing insights into platform stability, absorber performance, and overall system efficiency. By analyzing platform motions, wave absorber responses, and aerodynamic loading effects, this approach helps optimize the control strategies and structural design of hybrid offshore energy systems, ensuring enhanced power extraction and survivability under varying environmental conditions.

4. Results

This section compiles the principal findings. The results of each paper are presented in separate sections with a narrative that explains and contextualizes the results.

4.1 Paper I: Ballast optimization

Some parts of this section are reproduced from the author's licentiate thesis, Chapter 4.1[23].

4.1.1 Impact of ballast matter

The Figure 4.1 illustrates how the choice of ballast matter mass density influences the required ballast compartment size. It is observed that with larger ballast matter mass density, the area for the possible location of ballast CoG increases. It can also be seen that for heavier ballasts which correspond to smaller size compartments, it is possible to place ballast closer and farther away from the pivot point. This impacts the range of attainable inertia moments using ballast as depicted in Figure 4.2.

From Figure 4.3, the WA RAO is observed to increase slightly with a decrease in resonance frequency for larger inertia moments. The achievable range of resonance response is further investigated and shown in Figure 4.4. Comparing light to heavy ballast matter, results show an improvement in the resonance frequency range that can be reached when smaller ballast compartments, that correspond to heavier ballast (assuming the same rest angle is maintained), are used. The wide resonance frequency range appears to have a correlation with the possibility of placing smaller ballasts closer and farther from the pivot point.

4.1.2 Impact of compartment size

A comparison of the ballast inertia moments about the principal axis $I^*_{yy,b}$ relative to the ballast inertia moments $I_{yy,b}$ about the pivot point shows that the actual contribution of the ballast inertia moments $I^*_{yy,b}$ about the principal axis is less or equal to 1.4% of the ballast inertia

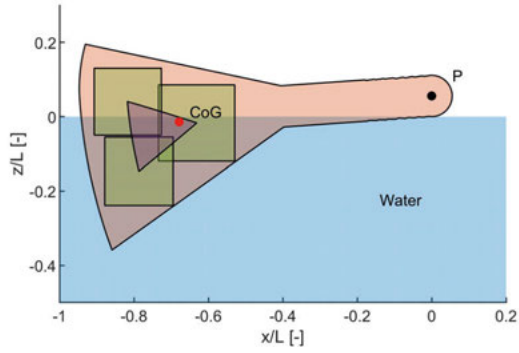

(a) Ballasts are found for a smaller matter mass density.

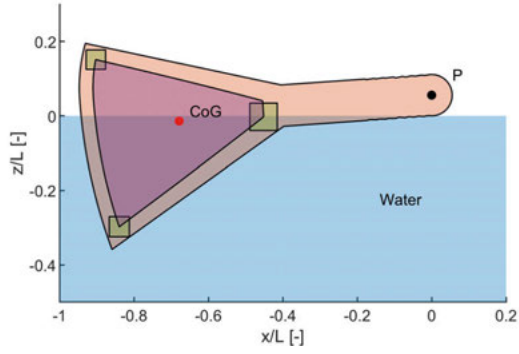

(b) Ballasts are found for a larger matter mass density.

Figure 4.1. Side view of the FPP wave absorber. The beige area denotes the absorber; the purple area inside it represents the area within which the ballast CoG can be located; the blue area indicates the calm seawater. Three green squares represent ballasts at different locations; only one ballast is enough for the given rest angle. The red dot marks the location of the empty absorber CoG; the black dot P is the pivot point. The scaling factor L is the total length of the absorber and its hinge-arm in the x-direction [56].

moment $I_{yy,b}$ about the pivot point. This validates the initial assumption that errors associated with differences in the ballast length $l_{yy,b}$ can be neglected. Figure 4.5 shows results at rest angles 4^o and 20^o for pivot point placement factor of 3.

4.1.3 Model validation

The analytical model presented in the previous subsections is validated using CAD numerical model. Using Solidworks©, the WA is modelled and a ballast combination search is performed to obtain the combined WA and ballast centre of gravity and inertia moment relative to the pivot

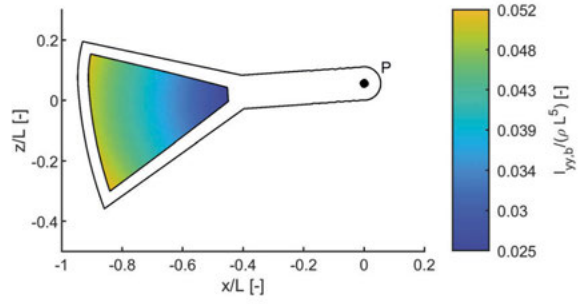

Figure 4.2. Inertia moments of the ballast compartments at different absorber locations were plotted as a function of the ballast CoGs [56].

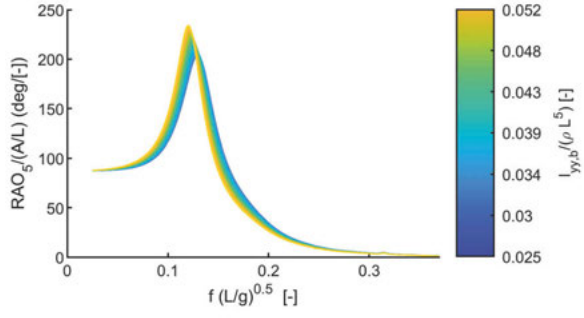

Figure 4.3. Normalized RAO of the wave absorber in pitch for all possible values of the ballast inertia moments, where the RAO curves are colour-coded by the ballast inertia moments [56].

point. Constraints in the search ensure that the ballast compartments can only be filled from the bottom up and the pivot point placement remains at 3. Results from the comparison between the analytical and CAD models for x and z components of the combined WA and ballast CoG are presented in Figures 4.6a and 4.6b. For the x-component, x_g, the results from both models agree closely. The z-component, z_g, results obtained from the CAD model appear relatively lower than that from the analytical model. This can be attributed to the approach of the ballast filling method used for the CAD model where the ballast compartments are filled from the bottom up and this constraint is not applied in the analytical model. The mass show marginally greater mass at increased rest angle which is likely a result of having the horizontal distance of the CoG from the pivot point at larger rest angles, hence the larger mass, Eqn (2.9). Conversely, a more significant difference is noticed for the

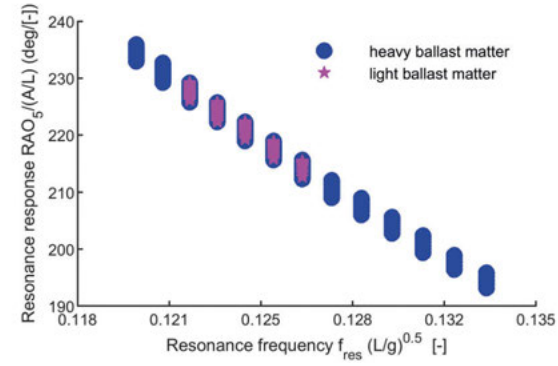

(a)

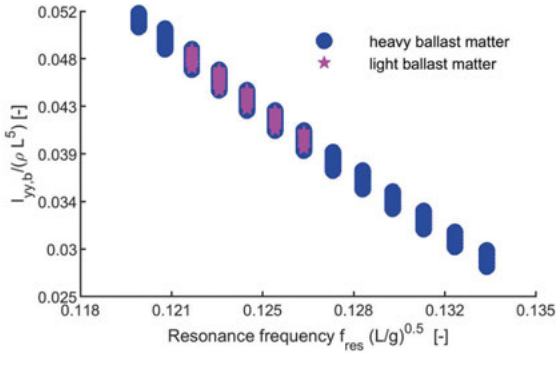

(b)

Figure 4.4. Impact of heavier and lighter ballast matters: (a) resonance response $\mathrm{RAO}_5/(A/L)$ plotted with respect to resonance frequency $f_{res}(L/g)^{0.5}$; (b) the ballast inertia moments $I_{yy,b}/(\rho L^5)$ plotted with respect to the resonance frequency $f_{res}(L/g)^{0.5}$ [56].

ballast inertia moments at higher rest angles (Fig. 4.7b). This difference is suspected to be due to numerical errors associated with the CAD software.

4.1.4 Power absorption performance: A case study

Three different sea states relevant to the North sea are used to demonstrate the application of the ballast optimization algorithm for power absorption performance. The chosen sea states have the same significant wave height but varied energy periods whose peaks are lower (SS1), coincide with (SS2) and higher (SS3) than the average resonance frequency of the WA as illustrated in Figure 4.9. For each case, the optimal PTO damping coefficient is used to ensure the maximization of the absorbed power. The Figure 4.8 shows the non-dimensional PTO damping coeffi-

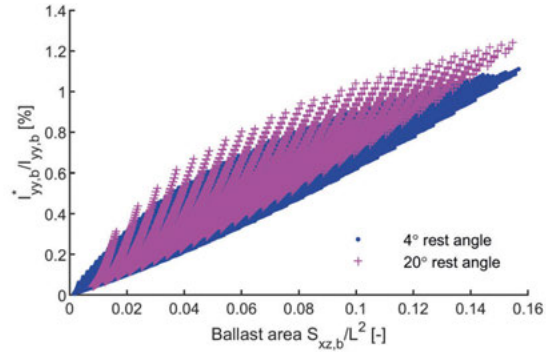

Figure 4.5. Actual contribution of the ballast inertia moments $I^*_{yy,b}$ about the principal axis to the ballast inertia moments $I_{yy,b}$ about the pivot point plotted with respect to the ballast cross-section area $S_{xz,b}/L^2$ [56].

cient for the absorber placement. It is observed, from Figure 4.10, that for SS1 increasing inertia moment makes the absorbed average power approach maximum. The opposite is the case for SS3. However, for SS2 average absorbed power reaches a maximum for one of the ballast inertia moments that occur when WA resonance frequency coincides with the sea state peak frequency. Another observation made is that the difference between the minimum and maximum values of the average absorbed power for various ballast inertia moments equals 35.9% for SS1, 3.5% for SS2 and 15.7% for SS3. This shows that there is a higher potential for adjusting the average absorbed power using ballasts for the sea state whose peak frequency is higher than the average WA resonance frequency. It could be more beneficial to design the WA ballast to have less variability in absorbed power between sea states, even if not all available power is absorbed. In Figure 4.11 the RAO variations at longer waves appear to be insignificant for various combinations of rest angle, pivot point placement and ballast inertia moments.

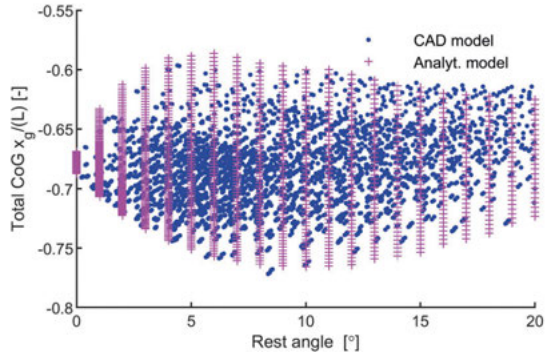

(a)

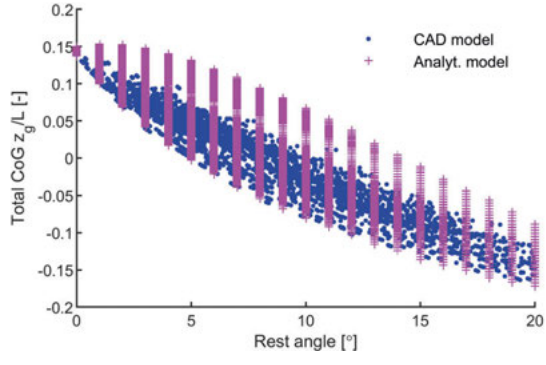

(b)

Figure 4.6. Comparison of the absorber and ballast mass properties calculated based on the CAD and analytical methods plotted against different rest angles of the absorber: (a) the x-component of the combined absorber and ballast CoG; (b) the z-component of the combined absorber and ballast CoG [56].

4.2 Paper II: Floating platform geometry optimization

Paper II applies a GA to maximize a floating platform's annual energy production (AEP) by adjusting up to ten geometric variables (V1–V10). Each geometry is analyzed with a potential-flow solver (WAMIT) to update hydrodynamic coefficients. The best-performing designs result in improved power capture with constraints such as static heel or trim angles.

Figure 4.12 compares single-variable sweeps around a base geometry. Variables like V1–V4 show stronger fitness influences, whereas others exhibit lesser effects. Figure 4.13(a) and (b) highlight that different initial populations can either accelerate or delay GA convergence. Some runs benefit from a partially optimized start, avoiding local optima.

Figure 4.14 addresses computation times per 100 GA iterations across different CPU core counts (4, 6, and 16) and varying numbers of vari-

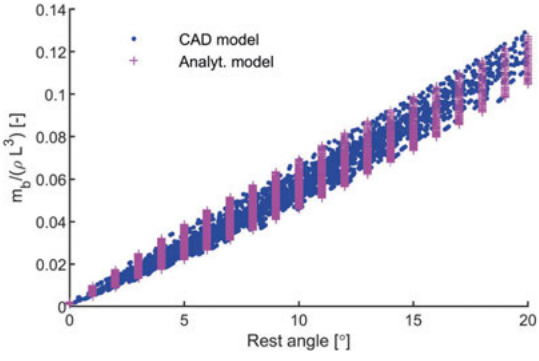

(a)

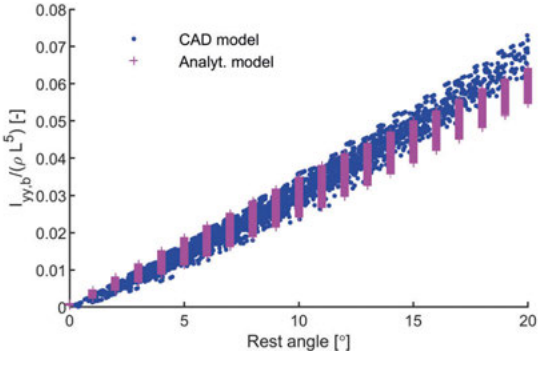

(b)

Figure 4.7. Comparison of the absorber and ballast mass properties calculated based on the CAD and analytical methods plotted against different rest angles of the absorber: (a) the ballast mass $m_b/(\rho L^3)$; (b) the ballast inertia moment $I_{yy,b/(\rho L^5)}$ [56].

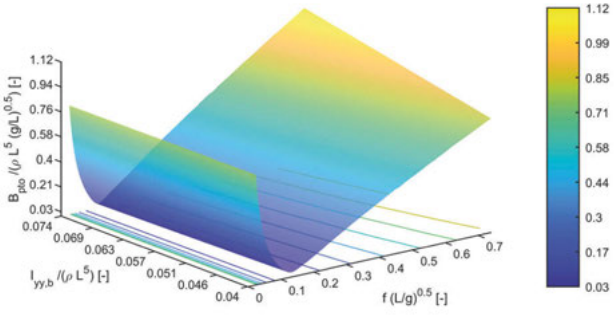

Figure 4.8. Non-dimensional PTO damping coefficient $B_{pto}/(\rho L^5(g/L)^{0.5})$ plotted with respect to wave frequency $f(L/g)^{0.5}$ and the ballast inertia moment $I_{yy,b}/(\rho L^5)$ [56].

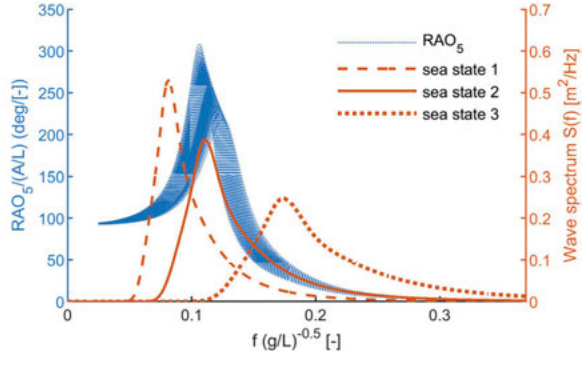

Figure 4.9. Wave spectra for three sea states and normalized RAOs of undamped absorber motion for different ballast inertia moments [56].

ables to optimize. Table 4.1 shows that WAMIT simulations dominate the runtime, comprising about 80% of the total. As the number of geometry variables grows, so does the solution space, thus prolonging GA convergence.

Table 4.1. *Explicit time usage for a single geometry analysis (WAMIT + MATLAB) under various computing power [21].*

	4 cores, 8 GB	**6 cores, 32 GB**	**16 cores, 128 GB**
WAMIT sim [s]	40	21	18
MATLAB pre/post [s]	10	6.2	5

Figure 4.15 reveals the distribution of solutions for 2 to 10 optimized variables, illustrating how expansions in the variable count affect the fitness outcomes. Figure 4.16(a) and (b) compare GA solutions when certain variables or variable ranges are curtailed vs. fully allowed. Con-

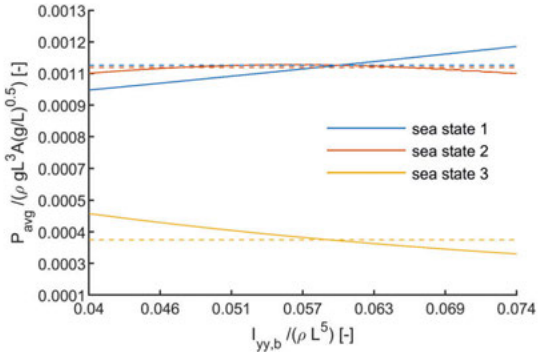

Figure 4.10. Dimensionless average absorbed power plotted with respect to the ballast inertia moments for the three sea states. The solid lines correspond to the inertia dependent average absorbed power and the dashed lines denote the average values across all ballast inertia moments [56].

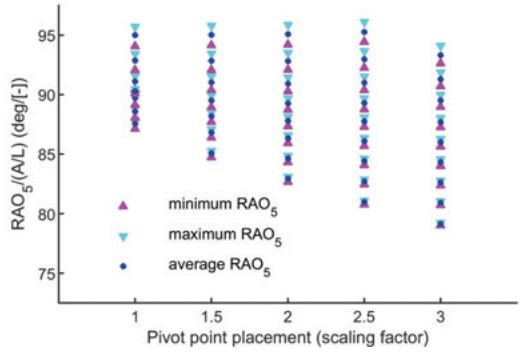

Figure 4.11. Maximum, minimum and average values of RAOs at zero frequency for different pivot point locations and different rest angles. Extrema and average values are taken across various ballast inertia moments. Six points corresponding to lower pivot point placement and greater rest angle are excluded from the plot due to full submersion of the absorber and incomparable hydrodynamic performance [56].

straining problematic ranges speeds convergence and yields better RAO responses.

Figure 4.17 exhibits different 6-variable configurations that end with fitness values within 0.03 of each other, establishing that no single global optimum emerges. Instead, multiple local optima produce near-equivalent performance.

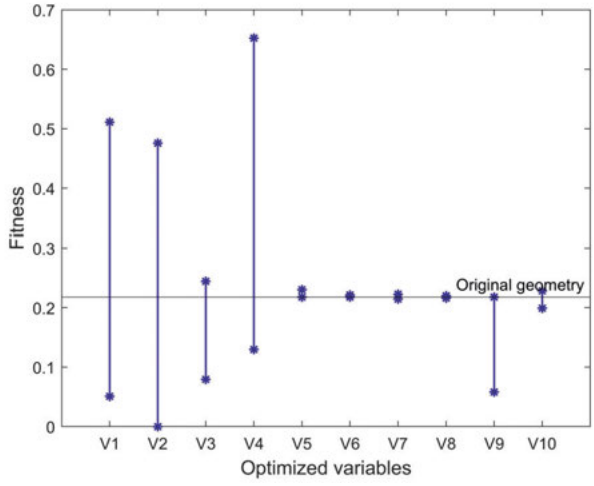

Figure 4.12. Parametric sweep of each geometry variable (V1–V10) from Paper II, measuring fitness changes around a baseline design. Certain variables prove more influential [21].

4.3 Paper III: ML-based wave–structure interaction predictions

Paper III proposes two machine-learning methods for predicting absorber pitch motion in a floating wind-wave system. One is a purely data-driven multi-step LSTM model; the other is a hybrid physics–ML approach that includes static hydrodynamic features (e.g., added mass) as inputs.

Table 4.2 compares mean squared error (MSE), mean absolute error (MAE), and R^2 for both models. The hybrid method achieves consistently lower error and higher R^2, affirming that physics-based features guide the network toward physically consistent predictions.

Table 4.2. *Performance metrics (Paper III) for the multi-step vs. hybrid models on training and validation sets [12].*

Dataset	**Model**	**MSE**	**MAE**	R^2
2***Training**	Multistep	0.00057	0.0163	0.9339
	Hybrid	0.00044	0.0139	0.9445
2***Validation**	Multistep	0.00038	0.0123	0.9111
	Hybrid	0.00026	0.0107	0.9439

Figure 4.18 shows how the multi-step network is more sensitive to perturbations in key input features, whereas the hybrid network retains stability by relying on additional physics-based data.

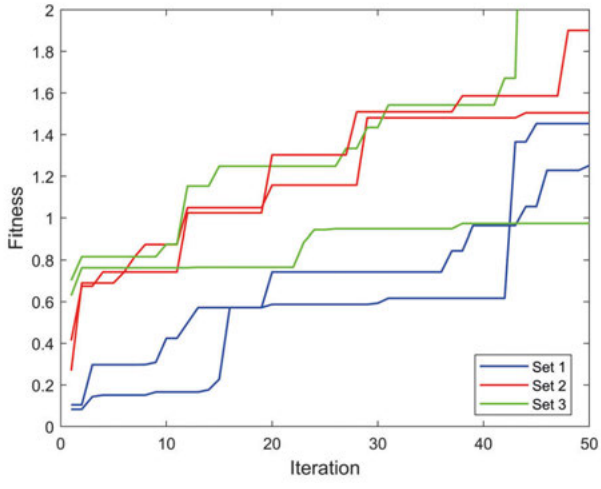

(a) Three distinct variable sets, each run twice, show different fitness plateaus.

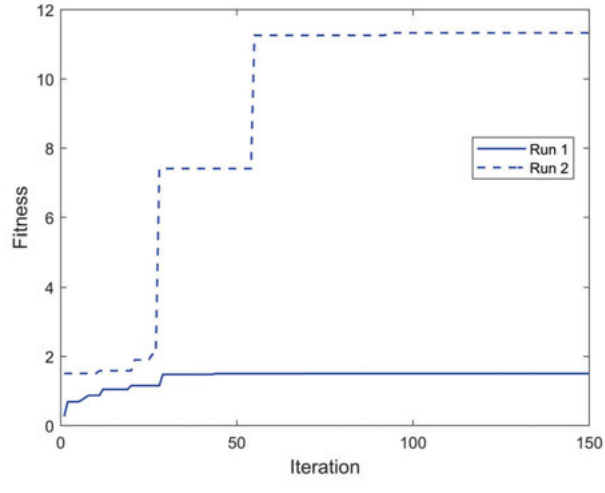

(b) Reusing a good geometry from run 1 as run 2's start yields rapid improvement.

Figure 4.13. GA search start points and their impact on convergence speed and final fitness [21].

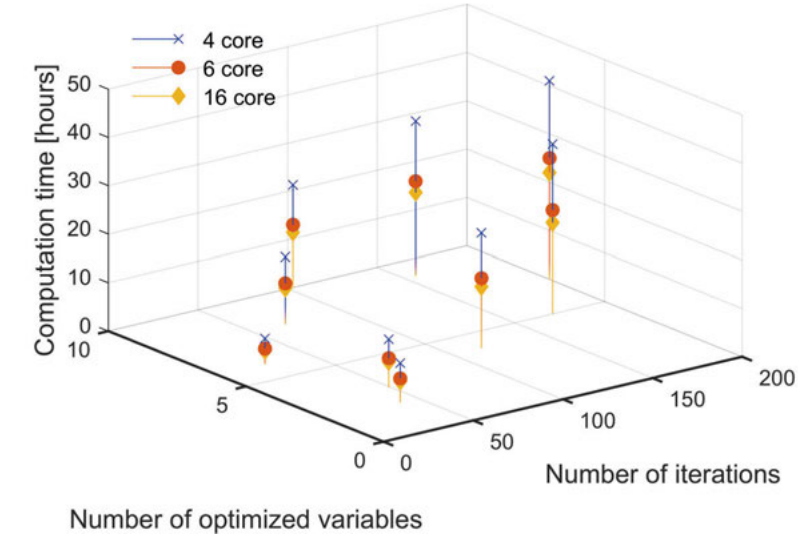

Figure 4.14. Computation time for GA convergence on 4-, 6-, and 16-core machines, as well as different variable counts. Larger solution spaces require more iterations [21].

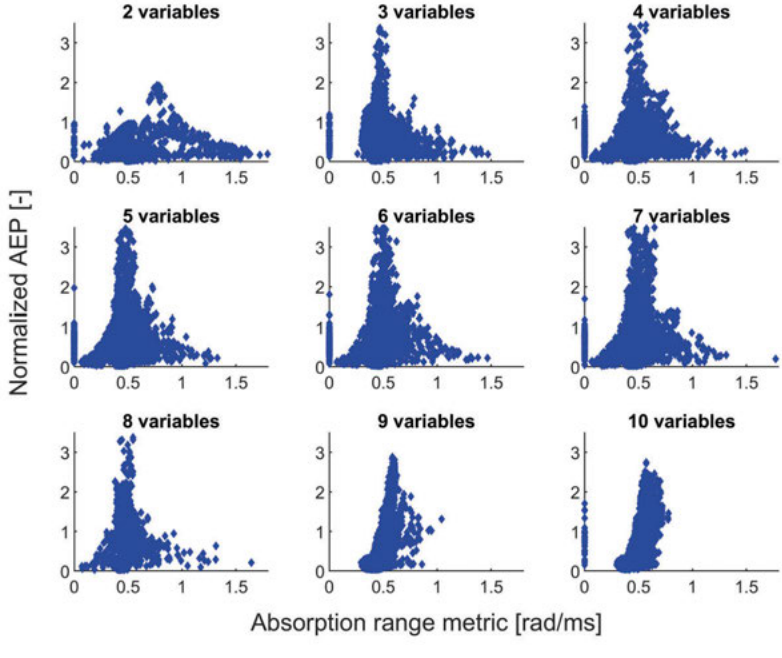

Figure 4.15. Solution space for different numbers of geometry variables, mapping absorption range vs. normalized AEP [21].

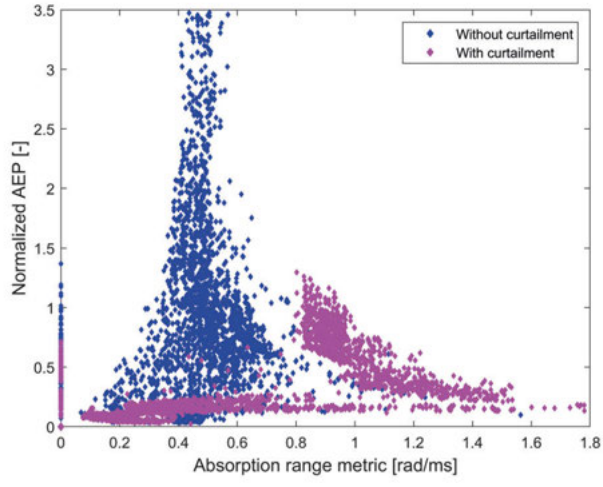

(a) With and without boundary curtailment on a 6-variable subset.

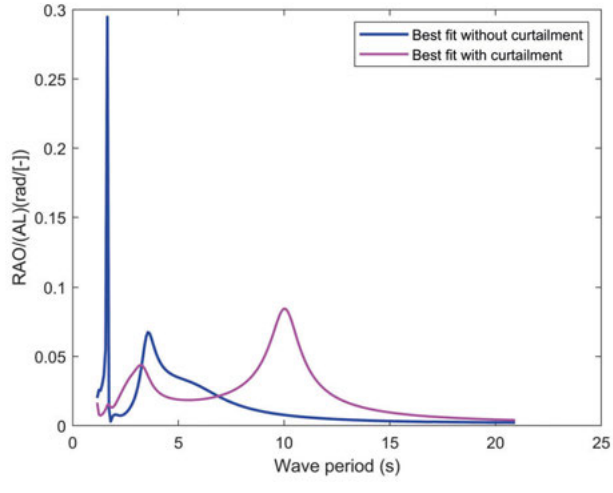

(b) RAO for the best geometry found, showing improved resonance placement with curtailment of negative variable ranges.

Figure 4.16. Comparison of GA results, indicating that restricting negative variable ranges can accelerate convergence and refine wave absorption [21].

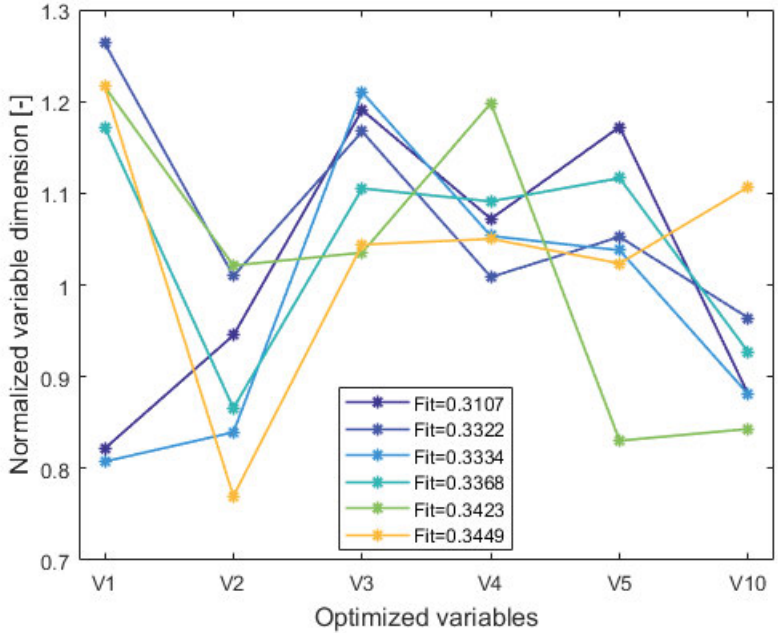

Figure 4.17. Different 6-variable combinations yielding final fitness values within 0.03. This indicates multiple local optima in the geometry space [21].

Figure 4.19 illustrates the prediction outcomes both before and after feature reduction. The corresponding scatter plots demonstrate how closely the predicted values match the actual values for both the multi-step and hybrid models. As indicated in Figure 4.19c, the multi-step model exhibits greater sensitivity to the removal of features. In contrast, while the hybrid model's reduced-feature predictions (Figure 4.19d) show less deviation from actual values than those of the multi-step model, its performance still diminishes when features are omitted. For the multi-step model, the wave spectrum and surge motion features are excluded, and for the hybrid model, wave spectrum, surge motion, and added mass features are removed. These selections are guided by the importance indicators shown in Figure 4.18.

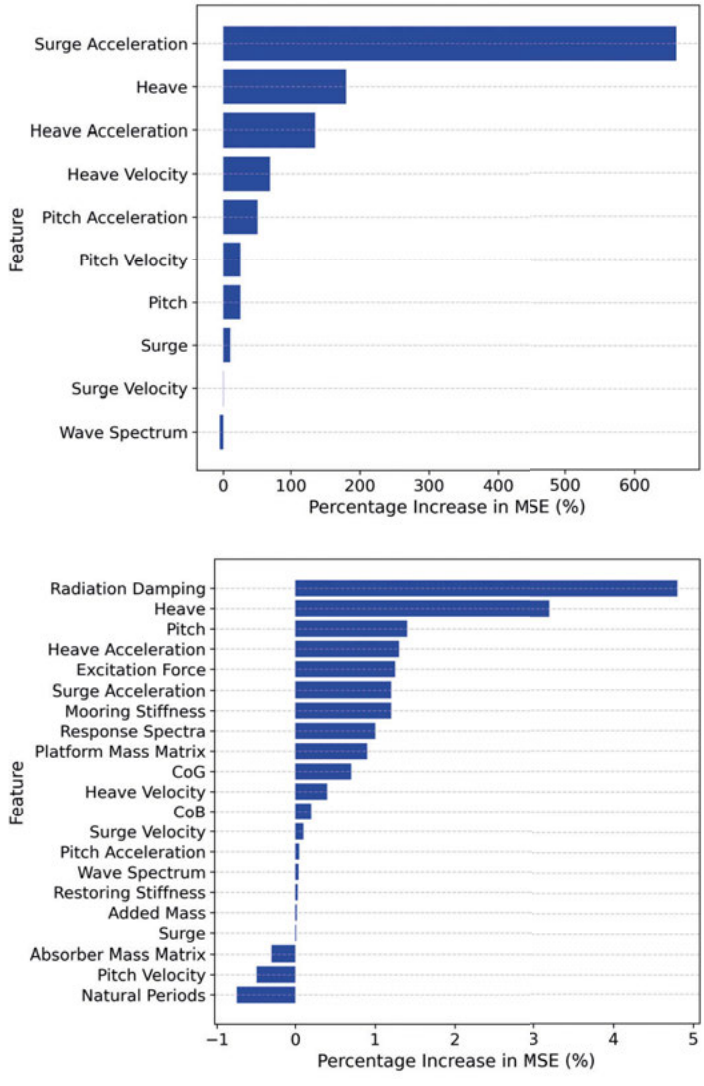

Figure 4.18. Feature importance for multi-step (top) and hybrid (bottom) models. The hybrid approach reduces deviation when crucial features are shuffled [12].

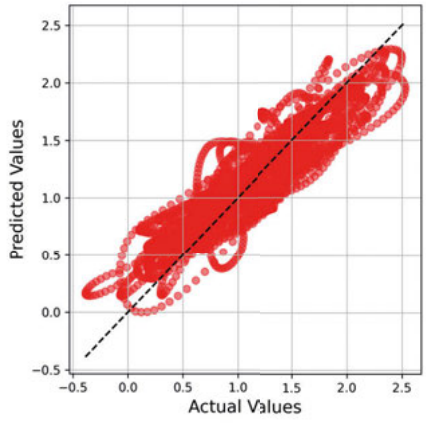

(a) Scatter Plot (Multistep Model)

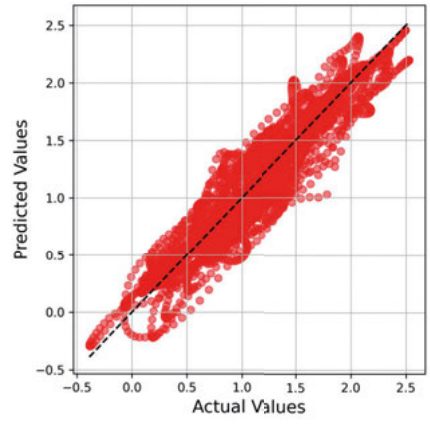

(b) Scatter Plot (Hybrid Model)

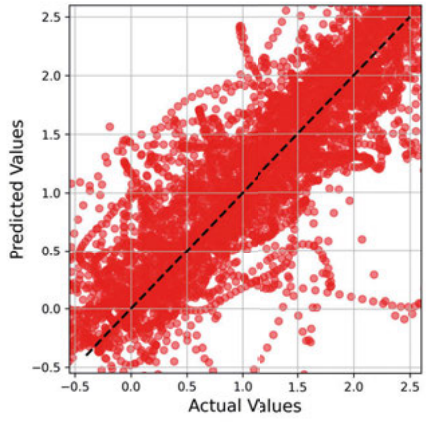

(c) Scatter Plot (Multistep Model, Reduced Features)

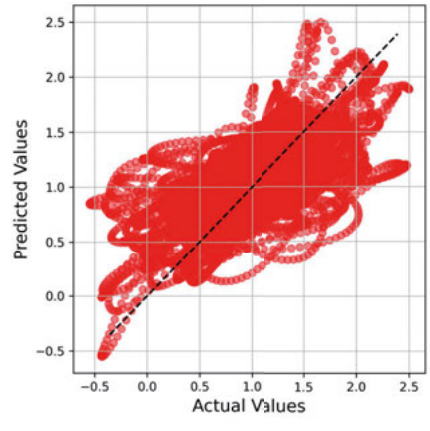

(d) Scatter Plot (Hybrid Model, Reduced Features)

Figure 4.19. Results before feature reduction: Actual vs P predicted scatter plots for the multistep and hybrid Models. Units are normalized [12].

Figure 4.20 depicts the wave spectra covered by training data (shaded region and purple line) vs. newly introduced wave states (red and green lines). Both models generalize fairly well to moderate extrapolations, though error margins grow for extremes. The results confirm that a data-driven or hybrid approach can reliably replicate wave-structure dynamics within the range of the training data set.

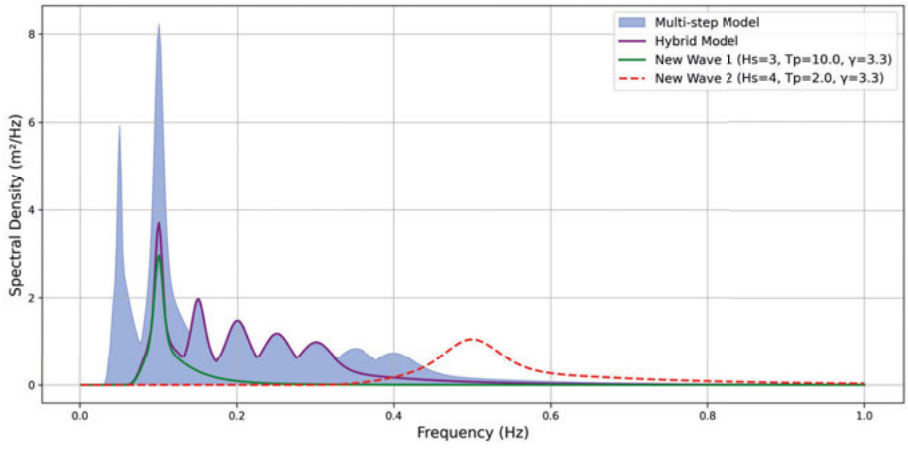

Figure 4.20. Wave spectra coverage (shaded and purple line) and two example of unseen wave distributions [12].

4.4 Paper IV: Permutation logic for multi-source offshore parks

Paper IV extends wave-energy optimization to a multi-source park of wind turbines, floating photovoltaics (OFPV), and wave converters feeding a common point of coupling (PCC). A genetic algorithm orchestrates partial or full curtailment (0%, 50%, 100%) to manage total energy losses, capacity factor, and seasonal mismatches.

Before applying the genetic algorithm to minimize energy losses at the point of common coupling (PCC), a discrete set of partial-disconnection states is defined for each renewable source. These states are derived from a logical framework similar to a 3–8 line decoder, extended to accommodate multiple fractional outputs. Table 4.3 outlines all 27 permutations, specifying the equation-based output for each decode pin. In this arrangement, each source (PV, wind, wave) may be combined or curtailed according to perc, which represents a user-defined fraction. This discrete logic ensures a manageable set of control actions for the GA to optimize, rather than continuous or infinite choices.

Figure 4.21 summarizes results from a five-year dataset near San Francisco Bay. Enabling partial disconnections in wave or wind, combined with OFPV, lowers the peak-to-average ratio substantially. Figure 4.22 plots energy losses against capacity factor (CF). Bipartite configurations manage a reasonable CF while minimizing losses, whereas some tripartite setups reach a high CF but incur greater overproduction or curtailment.

Figure 4.23a shows the total accumulated energy from each source during four representative months (January, April, July, October), show-

Table 4.3. *Proposed permutation logic based on a 3–8 line decoder (Paper IV) [52].*

Decode Pin	Permutation Logic (Equation-Based)
0	$\text{Output} = 0$
1	$\text{Output} = \text{perc} \cdot P_{\left(PV_{(\text{AC-side})}\right)}$
2	$\text{Output} = P_{\left(PV_{(\text{AC-side})}\right)}$
3	$\text{Output} = \text{perc} \cdot P_{\text{wind}}$
4	$\text{Output} = P_{\text{wind}}$
5	$\text{Output} = \text{perc} \cdot P_{\text{wave}}$
6	$\text{Output} = P_{\text{wave}}$
7	$\text{Output} = \text{perc}\left(P_{\left(PV_{(\text{AC-side})}\right)} + P_{\text{wind}}\right)$
8	$\text{Output} = \text{perc}\left(P_{\left(PV_{(\text{AC-side})}\right)}\right) + P_{\text{wind}}$
9	$\text{Output} = P_{\left(PV_{(\text{AC-side})}\right)} + \text{perc}\left(P_{\text{wind}}\right)$
10	$\text{Output} = P_{\left(PV_{(\text{AC-side})}\right)} + P_{\text{wind}}$
11	$\text{Output} = \text{perc}\left(P_{\left(PV_{(\text{AC-side})}\right)} + P_{\text{wave}}\right)$
12	$\text{Output} = \text{perc}\left(P_{\left(PV_{(\text{AC-side})}\right)}\right) + P_{\text{wave}}$
13	$\text{Output} = P_{\left(PV_{(\text{AC-side})}\right)} + \text{perc}\left(P_{\text{wave}}\right)$
14	$\text{Output} = P_{\left(PV_{(\text{AC-side})}\right)} + P_{\text{wave}}$
15	$\text{Output} = \text{perc}\left(P_{\text{wind}} + P_{\text{wave}}\right)$
16	$\text{Output} = \text{perc}\left(P_{\text{wind}}\right) + P_{\text{wave}}$
17	$\text{Output} = P_{\text{wind}} + \text{perc}\left(P_{\text{wave}}\right)$
18	$\text{Output} = P_{\text{wind}} + P_{\text{wave}}$
19	$\text{Output} = \text{perc}\left(P_{\left(PV_{(\text{AC-side})}\right)} + P_{\text{wind}} + P_{\text{wave}}\right)$
20	$\text{Output} = \text{perc}\left(P_{\left(PV_{(\text{AC-side})}\right)} + P_{\text{wind}}\right) + P_{\text{wave}}$
21	$\text{Output} = \text{perc}\left(P_{\left(PV_{(\text{AC-side})}\right)}\right) + P_{\text{wind}} + P_{\text{wave}}$
22	$\text{Output} = P_{\left(PV_{(\text{AC-side})}\right)} + \text{perc}\left(P_{\text{wind}} + P_{\text{wave}}\right)$
23	$\text{Output} = P_{\left(PV_{(\text{AC-side})}\right)} + P_{\text{wind}} + \text{perc}\left(P_{\text{wave}}\right)$
24	$\text{Output} = P_{\left(PV_{(\text{AC-side})}\right)} + \text{perc}\left(P_{\text{wind}}\right) + P_{\text{wave}}$
25	$\text{Output} = \text{perc}\left(P_{\left(PV_{(\text{AC-side})}\right)}\right) + P_{\text{wind}} + \text{perc}\left(P_{\text{wave}}\right)$
26	$\text{Output} = P_{\left(PV_{(\text{AC-side})}\right)} + P_{\text{wind}} + P_{\text{wave}}$

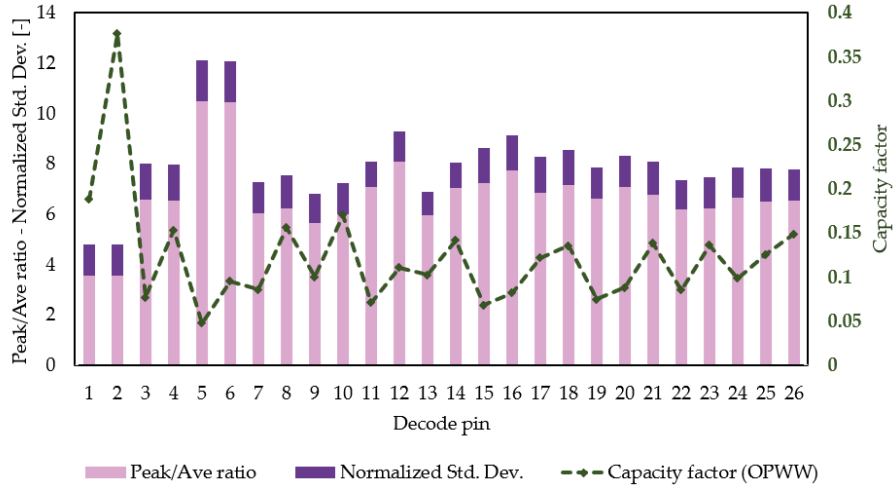

Figure 4.21. Five-year aggregator results with partial or full disconnection of wind, wave, or OFPV. Certain permutations drastically reduce power variability [52].

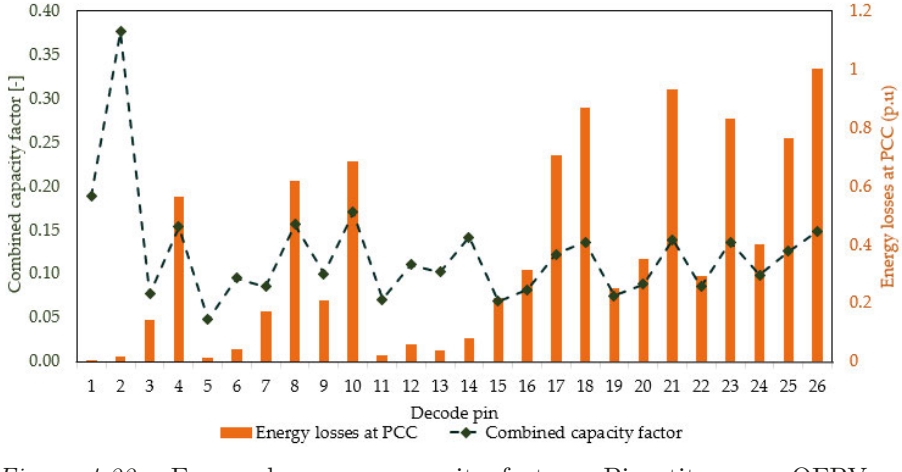

Figure 4.22. Energy losses vs. capacity factor. Bipartite wave–OFPV or wind–OFPV can offer moderate CF with reduced losses, while tripartite modes may have higher CF but larger losses [52].

ing how partial or full curtailment affects overall energy output from the aggregator. Figure 4.23b displays the corresponding energy losses at the PCC for each scenario, providing a direct comparison of the mismatch between supply and demand in each season. Figure 4.24 visualizes how each source, wind, wave, and PV, contributes to the final capacity factor when different permutation logic pins are activated, demonstrating how partial disconnection and synergy between sources play out across multiple months.

Table 4.4 presents the combined capacity factor before and after the genetic algorithm optimization, broken down by season (January, April, July, and October). This table quantifies the observed improvements and highlights how the capacity factor's range narrows following the single-objective function, yet energy losses at the PCC markedly decrease as a result of the optimized partial-disconnection schedules.

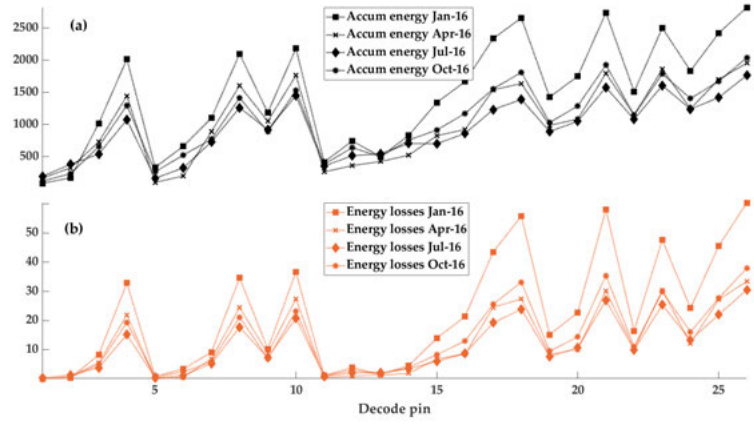

Figure 4.23. On the y-axis, seasonal (a) accumulated energy per source and (b) energy losses at the PCC for four selected months (January, April, July, October) in the multi-source park [52].

Table 4.4. *Combined capacity factor before and after seasonal optimization [52].*

Season	January	April	July	October	Std. Dev.
Before optimization	20.69%	14.34%	12.99%	15.44%	3.37
After optimization	9.69%	7.84%	7.27%	7.74%	1.07

Figures 12 and 13 in Paper IV (not shown here) illustrate the effect of a genetic algorithm that adaptively selects partial curtailment rules each season, which lowers overall losses but narrows the combined CF range. Figure 4.25 shows the seasonal losses before and after GA-based

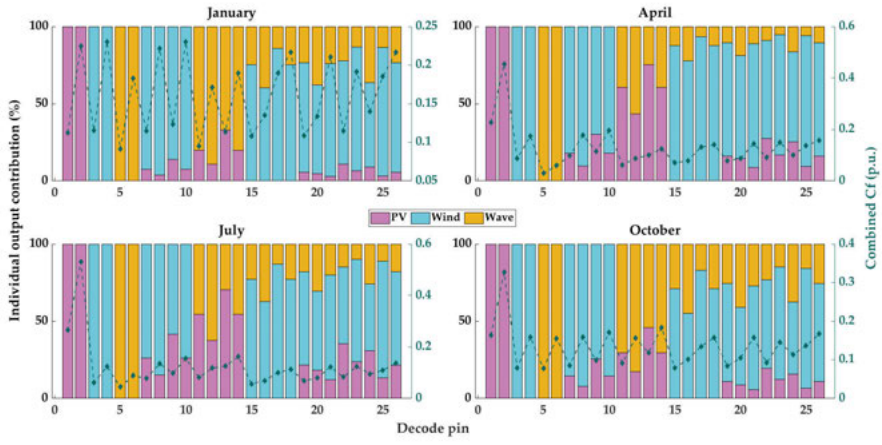

Figure 4.24. Seasonal comparison of each renewable energy source's contribution to the overall capacity factor under different permutation logic pins [52].

scheduling, with summer seeing minimal losses while spring remains higher due to limited demand.

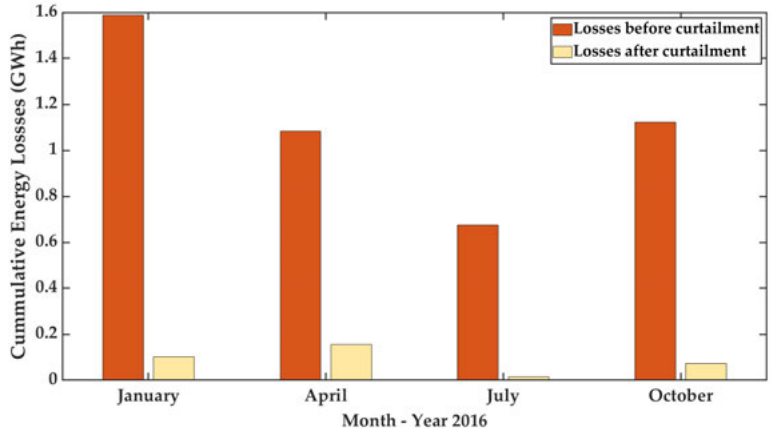

Figure 4.25. Seasonal energy losses at the PCC, comparing pre- and post-optimization scenarios. The GA substantially reduces losses during peak solar/wind months [52].

Table 4.5 presents different battery energy storage system (BESS) configurations for storing surplus. Offshore BESS arrangements reduce the need for large onshore transformers but require numerous battery strings. Onshore solutions use fewer parallel strings but at higher voltage levels, demanding more total batteries.

Overall, Paper IV demonstrates that a discrete curtailment logic, optimized via a GA, can coordinate multiple intermittent sources to reduce

Table 4.5. *Sizing of battery energy storage systems for three different onshore/offshore arrangements (Paper IV) [52].*

	Case 1	Case 2	Case 3
Battery rating	5 kW, 48 V	5 kW, 48 V	5 kW, 48 V
Main XF rating	40 MW, 6.6/66 kV	40 MW, 6.6/66 kV	40 MW, 6.6/66 kV
BESS XF rating	10 MW, 0.69/6.6 kV	10 MW, 0.69/6.6 kV	N/A
Connection side	0.69 kV	6.6 kV	66 kV
Location	Offshore	Offshore	Onshore
Series batteries	18	14	1375
Number of rows	64	85	4
Total batteries	1152	1190	5500

losses and maintain a reasonable capacity factor without large-scale storage. Further inclusion of BESS solutions refines this flexibility, with trade-offs in infrastructure cost and complexity.

4.5 Paper V: Coupled aero-hydrodynamic analysis

4.5.1 Wave absorber motion under different wind conditions

The absorber's dynamic response is examined under three wind scenarios: no wind, steady wind, and turbulent wind. With no wind, the wind speed is set to 1m/s which is below the cut-in wind speed of the wind turbine. In this case, the turbine remains idle and the absorber motion is governed solely by wave–platform interactions. Under steady wind, with wind speed set at 11.4m/s, constant rotor thrust modestly increases the absorber's pitch velocity, while turbulent wind, having a mean wind speed of 11.4m/s, introduces irregular fluctuations, yielding a lower sustained amplitude despite occasional peaks. Figure 4.26 shows the wind data used for this study. In Figure 4.27, the absorber's pitch velocity and instantaneous PTO power over a 1050 s window for these conditions are presented.

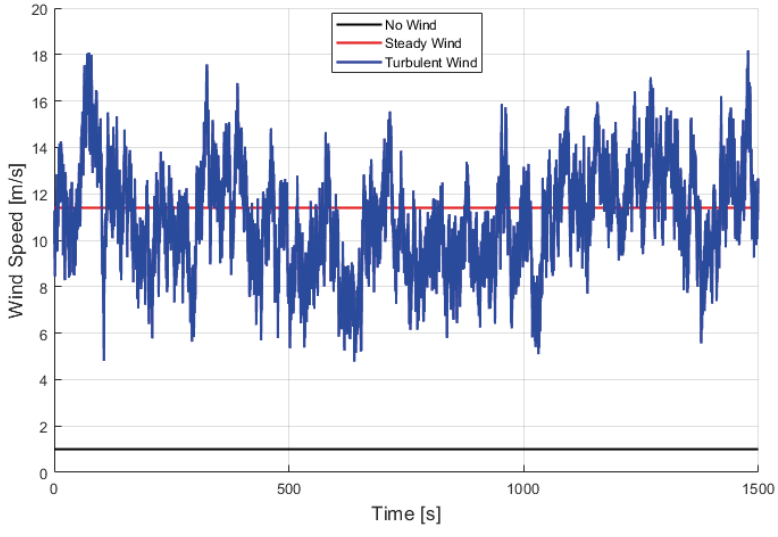

Figure 4.26. Wind data profiles used in the study: no wind, steady wind, and turbulent wind conditions [22].

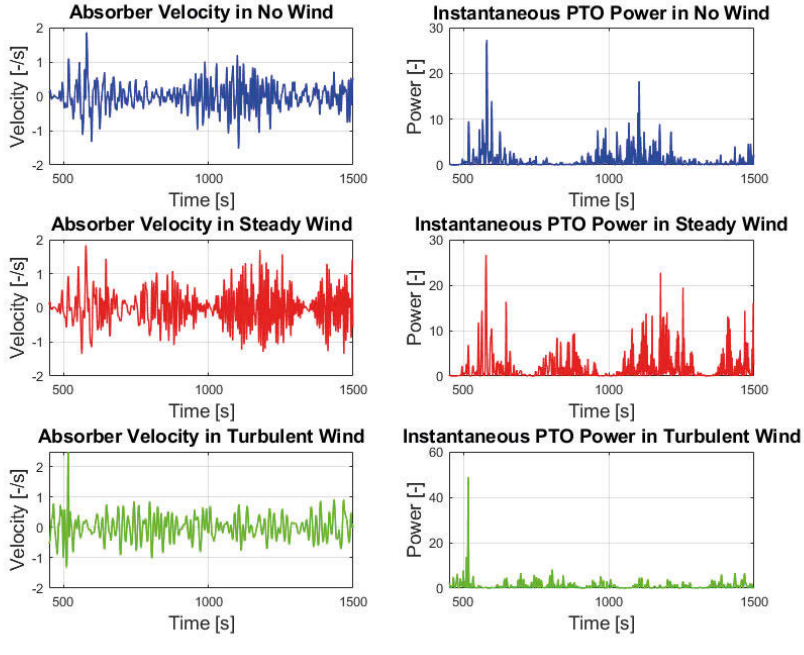

Figure 4.27. Comparison of absorber pitch velocity and instantaneous power under no wind, steady wind, and turbulent wind conditions[22].

The capture width ratio (CWR) is computed as the mean absorbed power normalized by the incident wave power per unit device width. Results indicate that under steady-wind conditions, the WEC resonates more effectively with the wave field, leading to the highest average CWR. In the turbulent wind case, the CWR is approximately 37% lower than in steady wind, while in the no-wind condition it is reduced by about 41%. Figure 4.28 summarizes the mean CWR across these scenarios.

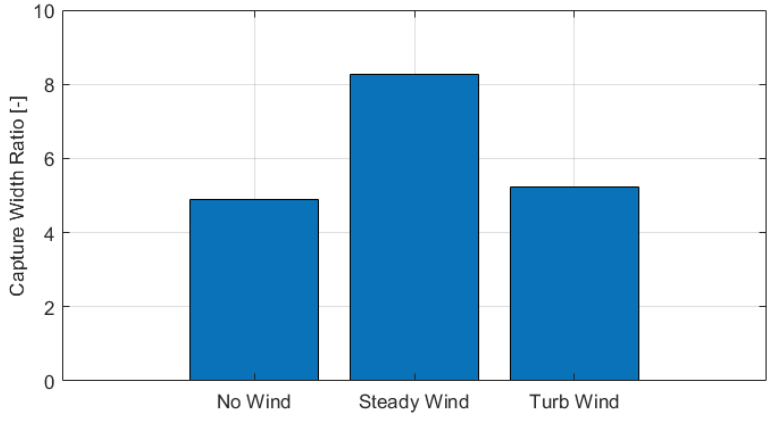

Figure 4.28. Comparison of absorber capture width ratio (CWR) under no wind, steady wind, and turbulent wind conditions [22].

Power spectral densities (PSDs) are estimated. In the no-wind case, a distinct peak appears near the dominant wave frequency, indicating strong resonance. With steady wind, the spectral peak shifts and its amplitude increases near 0.3 Hz, indicating a possible second resonance peak, induced by the wind flow. Turbulent wind produces a lower spectral peak. Figures 4.29 show the PSDs for the absorber heave and pitch, respectively.

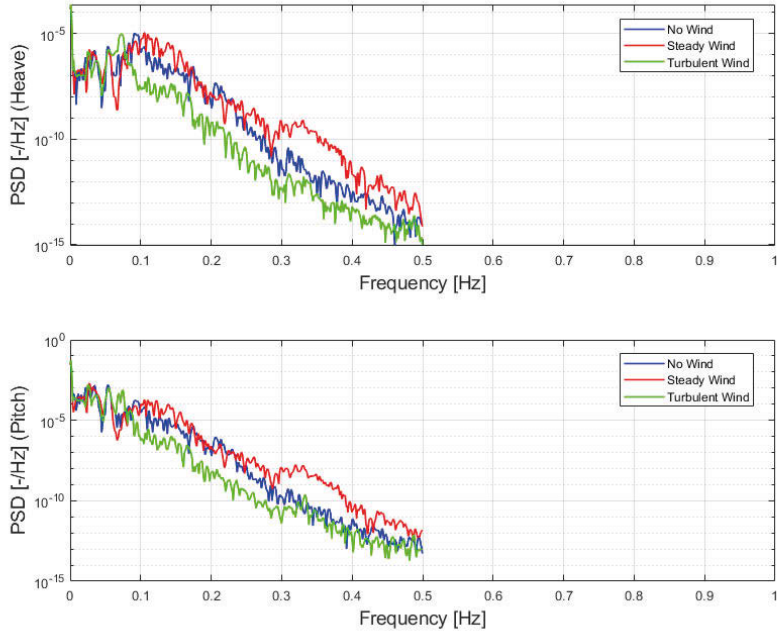

Figure 4.29. Absorber heave and pitch PSD under no wind, steady wind, and turbulent wind [22].

A comparison is made between normal turbine operation and a parked turbine state under turbulent wind. In normal operation, active blade pitch and torque control yield aerodynamic damping that stabilizes platform and absorber motions. When parked, the rotor is idle but still experiences significant thrust and torque. Figure 4.30 indicate that during normal operation, platform pitch amplitudes are reduced; noticeable changes occur around 342 seconds as the turbine transitions from idle to active operation.

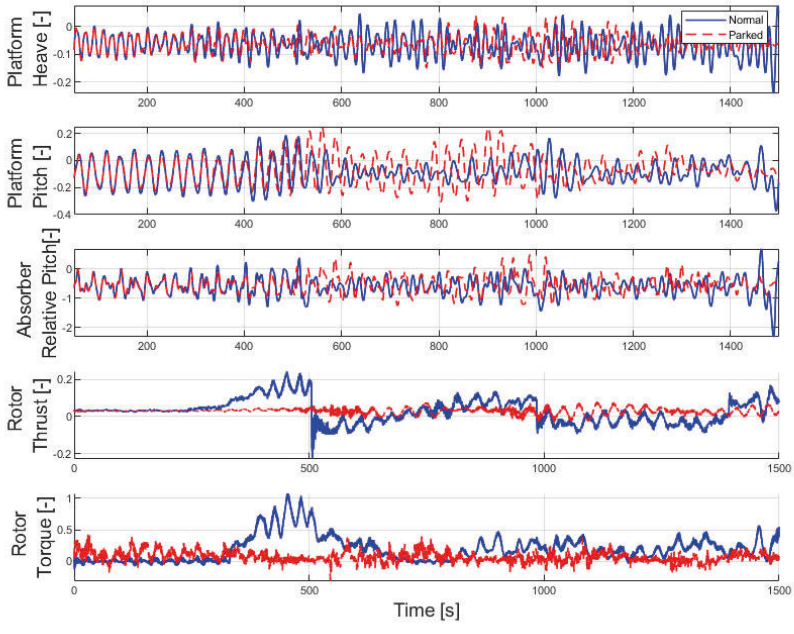

Figure 4.30. Time-domain comparison under turbulent wind for platform heave, pitch, and absorber relative pitch for normal operation versus a parked turbine [22].

Finally, RAOs (Figure 6 in **Paper V**, not shown here), indicate that turbine-induced aerodynamic forces have a negligible effect on resonance characteristics within the frequency range of interest.

Overall, the results of Paper V demonstrate the interplay between aerodynamic and hydrodynamic forces in a coupled wind–wave system. Wind conditions influence absorber dynamics and power capture, highlighting important considerations for system design and control.

5. Discussion

This chapter provides a critically analyzed synthesis of the research presented in the papers. Each paper addresses a distinct yet complementary topic within the realm of integrated floating wind–wave energy systems, from ballast-driven wave absorber tuning and platform geometry optimization to machine-learning (ML)–based performance prediction and multi-source aggregator control. By bringing these studies together, this discussion aims to scrutinize the methods, acknowledge limitations, and propose further refinements that can elevate the overall viability and efficiency of hybrid offshore energy devices.

Paper I demonstrates an analytical approach for selecting a wave absorber's ballast configuration in order to tune its resonance frequency. A key advantage is that the method only depends on the absorber's geometry and desired rest angle, thus avoiding the need for exhaustive parametric sweeps via numerical simulations. One strength here is the clear mathematical derivation linking the ballast mass distribution to the absorber's pitch inertia and hydrostatic balance. This stands in contrast to conventional trial-and-error methods in CAD or purely numerical simulations, which can be laborious.

However, the model's linear assumptions about wave-structure interactions may understate nonlinear effects, particularly for steep or extreme waves. While the paper validated the approach against CAD-based configurations for standard wave climates, real-world seas can deviate significantly, raising questions about stability or absorber performance outside the linear envelope. Future works may incorporate higher-order corrections or consider varying ballast dynamically across different sea states if operationally feasible.

Paper II relies on a genetic algorithm (GA) to optimize a floating platform's geometry for improved annual energy production (AEP). One notable insight from this study is that multiple local optima typically emerge, each yielding comparable AEP but differing in geometric parameters. This points to a non-convex design space where multiple designs might perform similarly within the same wave climate.

A potential issue arises when the number of viable design variables grows and the solution space becomes excessively large, thus requiring more iterations before convergence. Additionally, the frequency-domain framework utilized might not capture transient or nonlinear load cases, which could be crucial for structural design and survivability. While the

RAO-based approach and annualized metrics are effective for energy production, full system design necessitates a broader set of load and safety constraints. Balancing performance and manufacturability, or cost, could also become important future directions by including multi-objective cost-based GA targets.

Paper III's machine-learning strategies address a significant bottleneck: high-fidelity time-domain simulations can be computationally expensive when iterated over many design changes or control scenarios. By training a recurrent neural network (RNN), specifically a long short-term memory (LSTM) model, on simulation outputs,the paper shows that the absorber pitch motion can be forecast without re-running large simulations. The hybrid physics–ML model further leverages linear hydrodynamic coefficients to guide the network, yielding better accuracy and robustness than purely data-driven approaches.

Although promising for reducing computation time, one limitation is how well the trained models extrapolate to conditions beyond the training dataset. Extreme seas or unmodeled platform behaviors might challenge the ML method, causing larger prediction errors. Another concern is the potential for drifting accuracy over a device's operational life if wave conditions or the platform's mass distribution change significantly (due to fouling, wear, or ballast shifts). Incorporating online learning or scheduled retraining might mitigate these effects. Moreover, real-time deployment demands cautious model validation to ensure safe and stable operation under high-load or off-design conditions.

Paper IV explores a GA-based aggregator logic for partial disconnection of wind, wave, and floating PV sources at a single coupling point. This discrete approach is reminiscent of a digital multiplexer, allowing each source to be switched at 0%, 50%, or 100%. The crucial observation is that partial curtailment can curb surplus generation, reduce losses, and maintain a reasonable capacity factor with minimal storage, which is especially valuable in remote or island grids lacking robust infrastructure.

The discrete nature of the permutation logic facilitates a straightforward GA search, but also imposes rigid operational steps. Realizing more granular control than 50% might be beneficial for finer tuning, yet that would quickly expand the solution space. Additionally, the methodology presumes a known or predictable demand profile and wave/wind resource. Any substantial uncertainty or abrupt changes in conditions may require dynamic retuning, or a more adaptive aggregator that modifies permutations on-the-fly.

Battery energy storage system (BESS) sizing is considered as a complementary measure for surplus energy. However, the analysis would profit from more nuanced cost models and reliability assessments for large-scale deployment. The aggregator strategy may also be extended

to real-time or short-term forecasting of wind, wave, and solar resources, potentially integrated with machine-learning predictions (as introduced in Paper III).

Paper V extends the research by investigating the fully coupled, time-domain response of a floating wind–wave system using the `Fast2Aqwa`. While the integrated time-domain approach provides deeper insight into transient and coupled dynamics beyond the scope of linear or frequency-domain analyses (as used in Papers I and II), it also introduces new challenges. For instance, the reliance on BEM for aerodynamic loading inherently assume certain linearity and steady-state characteristics, which may not capture all nonlinear effects in extreme conditions. Additionally, the computational cost is significant for long-duration simulations.

When viewed together, these studies underscore the potential for comprehensive optimization and control in hybrid offshore energy systems. Paper I's ballast model and Paper II's geometry optimization each show how physical design changes can improve wave absorption, but each is limited by linear or frequency-domain approximations. Paper II complements these physical design methods by offering a time-domain or data-driven path to analyzing wave-structure interactions with far less computational cost. Paper IV brings the discussion full-circle by illustrating how discrete aggregator control can manage multiple renewables at a system scale, with partial disconnections effectively smoothing net power output. Paper V contributes to these approaches by providing detailed, time-domain analysis of the coupled aero-hydrodynamic behavior, revealing the dynamic interplay between wind turbine operation and wave energy capture.

One overarching theme is the tension between simplicity and accuracy. Papers I and II rely on linear potential-flow or analytical formulas to keep computations tractable, but at the cost of underrepresenting certain nonlinear phenomena. Paper III's data-driven approach partially mitigates that shortfall, though it requires extensive training data and careful validation. Paper IV's discrete aggregator logic is straightforward to implement and interpret, yet it may not fully exploit finer-grained curtailment options. Another unifying element is the role of the genetic algorithm: it appears in geometry optimization (Paper II) and aggregator logic (Paper IV) and could well be used in optimizing machine-learning hyperparameters or ballast compartments (Paper I), illustrating GA's flexibility in tackling non-convex solution spaces.

Overall, these studies convey strong indications that combining passive design (ballast distribution and platform geometry) with active data-driven control (machine-learning prediction and discrete aggregator logic) yields significant gains in energy capture, reduced losses, and operational adaptability. Yet challenges persist in scaling these methods to arrays of devices, extending them to harsher seas, and bridging the

gap between theoretical or site-specific wave climates and real-life environmental variability. Future work must also integrate techno-economic elements and structural reliability constraints to ensure that these optimizations lead to systems that are not only more efficient, but also economically feasible and robust in the long term.

6. Conclusion

This thesis has explored key design and control mechanisms to enhance the performance and viability of Floating Power Plant's (FPP) hybrid wind–wave concept, which combines a semi-submersible platform, a single wind turbine, and multiple pitching wave energy converters (WECs) equipped with hydraulic power take-offs (PTOs). The overarching aim was to systematically address how ballast distribution, platform geometry, data-driven forecasting, and multi-source aggregator controls can be integrated to improve both energy capture and operational stability.

A first strand of work established an analytical method for determining how ballast can be distributed within each pitching absorber to align its resonance frequency with the dominant wave climate. By relying primarily on the WEC's geometry and desired rest angle, this ballast-tuning framework (Paper I) circumvents exhaustive trial-and-error simulations. The method showed that resonance matching can meaningfully boost energy absorption, and it is sufficiently lightweight for rapid design studies.

Building on this, the geometry of the semi-submersible platform was optimized to maximize annual energy production (AEP) (Paper II). A genetic algorithm (GA) guided incremental design changes within a frequency-domain model, revealing multiple high-performing solutions that balance wave absorption, platform stability, and practical design constraints.

To address the computational burden of high-fidelity time-domain simulations and better capture nonlinear wave-structure interactions, a machine-learning (ML) approach was introduced (Paper III). By training a hybrid physics–ML model on outputs from high-fidelity simulation tools, the study demonstrated accurate short-term forecasting of WEC motion without repeatedly running expensive solvers. This data-driven method offers a powerful complement to frequency-domain analyses, especially for time-sensitive tasks such as real-time control or optimization.

In addition, the thesis examined how to manage multiple renewables, specifically wind, wave, and floating photovoltaics, under limited storage constraints (Paper IV). A discrete aggregator logic, also optimized by a GA, switched each source among 0%, 50%, or 100% output, thus reducing curtailment losses and smoothing power delivery when faced with changing resource or demand conditions. By partially disconnecting sources during surplus events, the system maintained a more favorable

capacity factor, demonstrating that integrated control schemes can be as critical as hardware design in achieving robust overall performance.

Finally, the extension of these concepts into a fully coupled aero-hydrodynamic framework (Paper V) provided a deeper understanding of the transient interactions between wind turbine operation and wave energy capture. FAST2AQWA combined hydrodynamic, aerodynamic, and structural models, illustrating the dynamic interplay between wind turbine controls, and platform/absorber dynamics. The results underscore that incorporating wind turbine thrust alters the behavior of the wave absorber.

Taken together, these contributions illustrate the value of combining analytical ballast-tuning formulas, GA optimization of platform geometry, hybrid physics–ML prediction,, discrete aggregator control and fully coupled wind-wave analysis. The work underscores that an end-to-end perspective, encompassing device-level tuning, platform-wide optimization, and multi-source power management, can enhance energy capture, mitigate downtime, and adapt to real-world resource variability.

7. Future work

The methodologies and results presented in this thesis highlight promising avenues for improving the performance of hybrid wind–wave energy systems. While substantial progress has been made, several open challenges and directions remain for future investigation:

Robust ballast and PTO strategies.
The ballast optimization studies focused on steady-state or mild wave conditions. Further work could explore adaptive or reconfigurable ballast systems that pump fluid among compartments in real time, matching evolving sea states. Similarly, beyond simple linear damping, power take-off (PTO) strategies might be extended to include advanced control schemes such as reactive or model-predictive control, where the ballast distribution and PTO damping could co-optimize energy capture across a wider bandwidth of frequencies.

Multi-objective GA for platform geometry.
The genetic algorithm approach in the platform geometry optimization was largely geared toward maximizing annual energy production (AEP) under specific constraints. Additional objectives, such as minimizing material cost, reducing environmental footprint, or maximizing structural longevity, could be integrated into a multi-objective framework. Incorporating manufacturing constraints or multi-phase design (where some platform components are fixed while others are variable) might further refine the search for practical commercial solutions.

Extended machine-learning models and real-time control.
The hybrid physics–ML models demonstrated improved accuracy and reduced computational time for wave-structure predictions. Future work could deploy these trained models in real-time operational settings, continuously updating forecasts of absorber motions and adjusting parameters in real time. Techniques like online learning, where the neural networks adapt to newly observed data from actual deployments, could further enhance predictive power and resilience to changing sea conditions.

Scaling up to large arrays and multi-WEC interactions.
The current investigations focused on one or a few wave absorbers integrated into a single platform. A natural extension involves analyzing interactions in larger arrays or multiple platforms moored near each other. Hydrodynamic coupling among neighboring WECs, collective mooring strategies, and aggregator-based partial disconnections across multiple platforms all raise new opportunities for system-level optimization and control.

Integration with grid and demand-side management.
Although permutation-based aggregator logic can minimize energy losses at the point of common coupling (PCC), further research could incorporate dynamic pricing, demand-side management, or grid ancillary services to maximize economic returns. Battery energy storage system (BESS) sizing could also be co-optimized with wave–wind generation profiles and grid constraints, especially for scenarios with islanded or microgrid operations.

Overall, the concepts and frameworks developed in this thesis lay a solid foundation for refining wave–wind integrated systems. By deepening our understanding of nonlinear hydrodynamics, enhancing adaptive control mechanisms, exploring larger-scale arrays, and addressing economic constraints, future research can help move these hybrid offshore technologies closer to widespread, commercially successful operation.

8. Summary of papers

This chapter briefly presents the core aims, methods, and contributions of the studies that collectively constitute the main body of this thesis.

Paper I

"Wave absorber ballast optimization based on the analytical model for a pitching wave energy converter"

This paper develops an analytical approach for determining an optimal ballast configuration in a pitching wave energy converter (WEC). The wave absorber is modeled so that the ballast compartments can be combined in various ways to shift the absorber's center of gravity and inertia, consequently tuning its resonance frequency to the prevailing wave climate. The method requires only knowledge of the wave absorber's geometry and its rest angle, making it computationally efficient compared to exhaustive CAD-based searches. Results demonstrate close agreement between the proposed method's predictions and validation runs from a full CAD model. This confirms that the analytical approach can identify suitable ballast placements without extensive iteration in simulation software.

The author's contributions include methodology, running simulations and validations, and drafting, reviewing and editing the manuscript. The article was published in the Journal of Ocean Engineering on 1 October 2021.

Paper II

"Geometry Optimization of a floating platform with an integrated system of wave energy converters using a genetic algorithm"

This paper applies a genetic algorithm (GA) to optimize the geometry of a semisubmersible-type platform carrying multiple pitching wave converters. An analytical low-order model of the platform was devised to ensure computational compatibility with iterative GA runs. The optimization problem focuses on maximizing the annual energy production (AEP) of the integrated wave absorbers while maintaining acceptable

hydrodynamic responses. The study also incorporates a measure of absorption range to ensure that the system operates effectively over a range of wave periods. The results show that the GA can discover configurations with broader absorption bandwidth, though the existence of multiple local maxima implies that no single global optimum emerges for the specified design variables. Results also show a viable means of curtailing the solution space-

The author's primary roles were in model development, running the simulation, analyzing the results, and writing the paper. The article was published in the Renewable Energy Journal of on 22 June 2024.

Paper III

"Machine learning techniques for efficient prediction of a wave energy converter's relative motion in a coupled wind and wave energy converter system"

This paper addresses the computational burden of high-fidelity wave-structure simulations by proposing machine-learning methods to predict the pitching absorber's motion. Two frameworks are introduced: a purely data-driven multi-step LSTM model and a hybrid physics–ML approach that combines linear hydrodynamic parameters (added mass, radiation damping) with a recurrent neural network. Both models are trained on time-series data from FAST2AQWA simulations. The hybrid model shows improved accuracy and robustness compared to the purely data-driven approach, particularly under unseen wave conditions or partial input feature removal. Results verify that these data-driven predictors can replace repeated time-domain simulations in iterative design processes, saving substantial computation time without sacrificing prediction fidelity.

The author did the model development, implementation, data acquisition, result analysis, and manuscript writing. This manuscript is currently under peer review.

Paper IV

"GA-Based permutation logic for grid integration of offshore multi-source renewable parks"

This paper extends the optimization scope to a larger multi-source park, including wind turbines, floating photovoltaics, and wave converters at a single point of common coupling. A discrete partial-disconnection logic is introduced, reminiscent of a 3–8 line decoder, allowing each source to be switched among 0%, 50%, or 100% output. The genetic al-

gorithm adapts the partial-connection permutations to minimize energy losses and balance capacity factor. The study uses a five-year dataset from an offshore site near San Francisco Bay. Simulation results show that selectively curtailing the most fluctuating sources (wind or wave) in partnership with OFPV significantly reduces peak-to-average ratios and overall losses. Seasonal optimization further refines these settings, while optional battery storage sizing is examined to store surplus power.

The author's roles involved methodology, running the GA-based aggregator simulations, and analyzing results, and reveiwing draft and visualization. The paper is published in *Machines*, 7 December 2022.

Paper V

"Time-domain analysis of aero-hydro interactions on floating offshore platform with co-located wind turbine and wave energy converters"

This paper develops a fully coupled, time-domain analysis in FAST2AQWA that uses convolution integrals to capture radiation-memory effect for time integration. The model simulates the dynamic interactions between a wind turbine and multiple pitching WECs on a floating platform.

Analysis of how varying wind conditions (no wind, steady wind, and turbulent wind) affect absorber and platform dynamics is presented. Additionally, a comparison is also made for normal turbine operation versus a parked state under turbulent wind. The results highlight what factors should be taken into account when designing or optimizing the systems' control.

The author did the model development, implementation, data acquisition, result analysis, and manuscript writing. This manuscript is currently under peer review.

9. Svensk sammanfattning

Denna avhandling handlar om hur olika förnybara energikällor kan samverka och på så sätt öka den totala energiproduktionen. Den hydrodynamiska interaktionen mellan hybrida vind- och våg-energiomvandlingssystem har studerats. Den första delen av avhandlingen undersöker hur massfördelningen och positionen för en vågabsorbator kan anpassas till och möjliggöra passiv rörelsekontroll för att absorbera mer vågenergi. Ett geometrisk optimeringsramverket är utvecklat för en halvt nedsänkbar plattform som använder genetisk algoritm för att identifiera designparametrar som maximerar kraftgenereringen genom att optimera den relativa rörelsen mellan plattformen och integrerade vågabsorbenter. Forskningen betonar ytterligare vikten av tillförlitliga vågabsorberingsmodeller, som visar hur robusta prognoser. Med hjälp av maskininlärning kan metoder tillämpas för att anpassa systemet för varierande oceaniska förhållanden. I den sista studien studeras en park med flera olika förnybara offshoreenergikällor, den omfattar vindkraftverk, flytande solceller och vågkraftverk. En permutationsbaserad aggregatorlogik, inspirerad av en 3–8 rads avkodare och optimerad med hjälp av en genetisk algoritm, möjliggör partiell eller fullständig begränsning av enskilda energikällor i diskreta steg. Denna strategi minimerar energiförluster vid den gemensamma inkopplingspunkten och balanserar kapacitetsfaktorn. Resultaten visar på att ett integrerat tillvägagångssätt, som kombinerar analytiska modeller, numeriska simuleringar och avancerade optimeringstekniker, avsevärt kan förbättra vågenergiutvinning, systemstabilitet och det övergripande årliga energiutbytet.

10. Acknowledgement

I would like to express my deepest gratitude to my supervisors, Irina Temiz and Andrej Savin. Irina, thank you for your continuous support, insightful advice, unwavering encouragements and mentorship throughout this journey. Your guidance has been invaluable. Andrej, I truly appreciate all your help, and the ease of working with you.

Many thanks to the team at Floating Power Plant for your collaboration and support. It has been a pleasure working with you.

To my wonderful colleagues and office mates, Aisuulu, Hasupama, Imran, Jessica, Rina, thank you for your comradeship. A hearty thank you to Aisuulu, Imran, and Rina, who were always ready to assist whenever I worked remotely and faced unexpected computer shutdowns. I truly appreciate your help in turning it back on whenever I called. To Anar, your friendship means a lot to me, and I am deeply grateful for your kindness and encouragement.

Olle, I appreciate your help with translating my 'Svensk sammanfattning', and for our many interesting conversations, it has been a rewarding experience.

To my dear Jane Temi, you were always literally just one phone call away, thank you for always being ready to help in every way possible.

To my family, thank you for your unconditional love and support throughout this journey. Your encouragement and belief in me have been a driving force in my success.

A very special thank you to my mother-in-law, Anthonia Umeh, for taking good care of Adimchi while I worked on this thesis. Your support has been priceless and I am forever grateful.

To Adimchinobi, when you learn to read this, I want you to know that you are my muse and my greatest source of happiness. Your presence has brought me endless joy and motivation.

Finally, to Ifeanyi, thank you for being an amazing best friend and for always believing in me.

I also extend my gratitude to Uppsala University, Sweden, STandUP for Energy, the OESA project, the European Regional Development Fund (ERDF) within the Interreg North Sea Region Programme 2015–2020, EU SCORES, and the Swedish Energy Agency (PA no. 48347-1) for co-financing these studies and making this research possible.

11. References

[1] Raju Ahamed, Kristoffer McKee, and Ian Howard. A review of the linear generator type of wave energy converters' power take-off systems. *Sustainability*, 14(16):9936, 2022.

[2] Elie Al Shami, Ran Zhang, and Xu Wang. Point absorber wave energy harvesters: A review of recent developments. *Energies*, 12(1):47, 2018.

[3] A. Babarit. A database of capture width ratio of wave energy converters. *Renewable Energy*, 80:610–628, 2015.

[4] A. Babarit. *A Unified Theoretical and Experimental Investigation of Wave Energy Converters*. Springer, 2017.

[5] A. Babarit. *Ocean Wave Energy Conversion: Resource, Technologies and Performance*. Elsevier, 2020.

[6] AbuBakr S Bahaj. Generating electricity from the oceans. *Renewable and Sustainable Energy Reviews*, 15(7):3399–3416, 2011.

[7] Giovanna Bevilacqua and Barbara Zanuttigh. Overtopping wave energy converters: general aspects and stage of development. 2011.

[8] Paolo Boccotti. Comparison between a u-owc and a conventional owc. *Ocean Engineering*, 34(5-6):799–805, 2007.

[9] A. G. L. Borthwick. Wave energy converters and their environmental impact. *Energy & Environment*, 18:561–582, 2007.

[10] A. G. L. Borthwick. Marine renewable energy seascape. *Engineering*, 2(1):69–78, 2016.

[11] Kjell Budal and Johannes Falnes. Wave power conversion by point absorbers: A norwegian project. *International Journal of Ambient Energy*, 3(2):59–67, 1982.

[12] Andrej Savina Irina Temiza Chisom Ekweobaa, Lander Galera. Machine learning techniques for efficient prediction of a wave energy converter relative motion in a coupled wind and wave energy converter system. Unpublished manuscript, 2025.

[13] A. Clément, P. McCullen, A. F. de O. Falcão, et al. Wave energy in europe: Current status and perspectives. *Renewable and Sustainable Energy Reviews*, 6(5):405–431, 2002.

[14] Pasquale Contestabile, Gaetano Crispino, Enrico Di Lauro, Vincenzo Ferrante, Corrado Gisonni, and Diego Vicinanza. Overtopping breakwater for wave energy conversion: Review of state of art, recent advancements and what lies ahead. *Renewable Energy*, 147:705–718, 2020.

[15] Pasquale Contestabile, Vincenzo Ferrante, Enrico Di Lauro, and Diego Vicinanza. Prototype overtopping breakwater for wave energy conversion at port of naples. In *ISOPE International Ocean and Polar Engineering Conference*, pages ISOPE–I. ISOPE, 2016.

[16] Brian M Count and Takeaki Miyazaki. Study on floating attenuator wave energy devices. *Journal of the Society of Naval Architects of Japan*, 1984(155):164–171, 1984.
[17] Balazs Czech and Pavol Bauer. Wave energy converter concepts: Design challenges and classification. *IEEE Industrial Electronics Magazine*, 6(2):4–16, 2012.
[18] Oskar Danielsson. *Wave energy conversion: linear synchronous permanent magnet generator*. PhD thesis, Acta Universitatis Upsaliensis, 2006.
[19] Frédéric Dias, Emiliano Renzi, Sarah Gallagher, Dripta Sarkar, Yanji Wei, Thomas Abadie, Cathal Cummins, and Ashkan Rafiee. Analytical and computational modelling for wave energy systems: the example of oscillating wave surge converters. *Acta Mechanica Sinica*, 33:647–662, 2017.
[20] Benjamin Drew, Andrew R Plummer, and M Necip Sahinkaya. A review of wave energy converter technology, 2009.
[21] Chisom Ekweoba, Dan El Montoya, Lander Galera, Susana Costa, Sarah Thomas, Andrej Savin, and Irina Temiz. Geometry optimization of a floating platform with an integrated system of wave energy converters using a genetic algorithm. *Renewable Energy*, 231:120869, 2024.
[22] Chisom Ekweoba, Dan El Montoya, Lander Galera, Susana Costa, Andrej Savin, and Irina Temiz. Time-domain analysis of aero-hydro interactions on floating offshore platform with co-located wind turbine and wave energy converters. Unpublished manuscript. Department of Electrical Engineering, Uppsala University, Box 65, 75103 Uppsala, Sweden; Floating Power Plant A/S, Park Alle 382, Vallensbæk, 2625, Denmark, 2025.
[23] Chisom Miriam Ekweoba. Hydro-mechanical optimization of a wave energy converter, 2022.
[24] A. F. de O. Falcão. Wave energy utilization: A review of the technologies. *Renewable and Sustainable Energy Reviews*, 14(3):899–918, 2010.
[25] AF de O Falcão. The shoreline owc wave power plant at the azores. In *Proceedings of 4th European Wave Energy Conference*, pages 42–47, 2000.
[26] J. Falnes. *Ocean waves and oscillating systems: linear interactions including wave-energy extraction*. Cambridge University Press, UK, 2002.
[27] C. Fitzgerald and L. Bergdahl. Including mooring dynamics in the assessment of a floating wave energy converter. *Proc. IMechE Part M: J. Eng. Maritime Environ.*, 221(4):81–91, 2007.
[28] M. Folley, editor. *Numerical Modelling of Wave Energy Converters: State-of-the-Art Techniques for Single Devices and Arrays*. Springer, 2012.
[29] Matt Folley, Trevor Whittaker, and Max Osterried. The oscillating wave surge converter. In *ISOPE International Ocean and Polar Engineering Conference*, pages ISOPE–I. ISOPE, 2004.
[30] Spyros Foteinis. Wave energy converters in low energy seas: Current state and opportunities. *Renewable and Sustainable Energy Reviews*, 162:112448, 2022.

[31] Y. Gao, T. Zheng, and G. Wu. Nonlinear wave loads and motions of a moored floating wec. *Applied Ocean Research*, 95:102011, 2020.
[32] Y. Gao, T. Zheng, and G. Wu. Nonlinear wave loads and motions of a moored floating wec. *Applied Ocean Research*, 95:102011, 2020.
[33] Bingyong Guo, Tianyao Wang, Siya Jin, Shunli Duan, Kunde Yang, and Yaming Zhao. A review of point absorber wave energy converters. *Journal of Marine Science and Engineering*, 10(10):1534, 2022.
[34] R. Henderson. Design, simulation, and testing of a novel hydraulic power take-off system for the pelamis wave energy converter. *Renewable Energy*, 31(2):271–283, 2006.
[35] Ross Henderson. Design, simulation, and testing of a novel hydraulic power take-off system for the pelamis wave energy converter. *Renewable energy*, 31(2):271–283, 2006.
[36] Yue Hong. *Numerical Modelling and Mechanical Studies on a Point Absorber Type Wave Energy Converter*. PhD thesis, Acta Universitatis Upsaliensis, 2016.
[37] Irina A Ivanova, Olov Agren, Hans Bernhoff, and Mats Leijon. Simulation of wave-energy converter with octagonal linear generator. *IEEE Journal of Oceanic Engineering*, 30(3):619–629, 2005.
[38] L. Johanning, G. H. Smith, and J. Wolfram. Mooring design approach for wave energy converters. *Proc. IMechE Part M: J. Eng. Maritime Environ.*, 221(4):81–91, 2007.
[39] John Magne Johnsen and Ola Øritsland. Design and optimisation of taut-leg mooring systems. In *Offshore Technology Conference*, pages OTC–10776. OTC, 1999.
[40] Mohd Afifi Jusoh, Mohd Zamri Ibrahim, Muhamad Zalani Daud, Aliashim Albani, and Zulkifli Mohd Yusop. Hydraulic power take-off concepts for wave energy conversion system: A review. *Energies*, 12(23):4510, 2019.
[41] B. Kinsman. *Wind Waves: Their Generation and Propagation on the Ocean Surface*. Prentice-Hall, 1965.
[42] Jens Peter Kofoed, Peter Frigaard, Erik Friis-Madsen, and Hans Chr Sørensen. Prototype testing of the wave energy converter wave dragon. *Renewable energy*, 31(2):181–189, 2006.
[43] Iraide López, Jon Andreu, Salvador Ceballos, Iñigo Martínez De Alegría, and Iñigo Kortabarria. Review of wave energy technologies and the necessary power-equipment. *Renewable and sustainable energy reviews*, 27:413–434, 2013.
[44] Lucia Margheritini, Diego Vicinanza, and Peter Frigaard. Ssg wave energy converter: Design, reliability and hydraulic performance of an innovative overtopping device. *Renewable Energy*, 34(5):1371–1380, 2009.
[45] Joseph J Monaghan. Smoothed particle hydrodynamics and its diverse applications. *Annual Review of Fluid Mechanics*, 44(1):323–346, 2012.
[46] Markus Mueller and Robin Wallace. Enabling science and technology for marine renewable energy. *Energy policy*, 36(12):4376–4382, 2008.
[47] Arvid Naess, Arvid Næss, and Torgeir Moan. *Stochastic dynamics of marine structures*. Cambridge University Press, 2013.

[48] Dezhi Ning, Yu Zhou, and Chongwei Zhang. Hydrodynamic modeling of a novel dual-chamber owc wave energy converter. *Applied ocean research*, 78:180–191, 2018.

[49] SS Prakash, KA Mamun, FR Islam, Rishaal Mudliar, Cherie Pau'u, Manasa Kolivuso, and Semi Cadralala. Wave energy converter: a review of wave energy conversion technology. In *2016 3rd Asia-Pacific World Congress on Computer Science and Engineering (APWC on CSE)*, pages 71–77. IEEE, 2016.

[50] Xiang Rao, Bijun Wu, Pei-yu Liu, Fuming Zhang, and Zhiwen Yuan. High conversion efficiency of oscillating-buoy wec with pneumatic pto: Principle analysis and experimental verification. *Available at SSRN 4780088*.

[51] J. V. Ringwood, G. Bacelli, and F. Fusco. Energy-maximizing control of wave-energy converters: The development of control system technology to optimize their operation. *IEEE Control Systems Magazine*, 34(5):30–55, 2014.

[52] Brenda Rojas-Delgado, Chisom Ekweoba, George Lavidas, and Irina Temiz. Ga-based permutation logic for grid integration of offshore multi-source renewable parks. *Machines*, 10(12):1208, 2022.

[53] L. Rusu and C. Guedes Soares. Numerical modeling to estimate the spatial distribution of wave energy in the portuguese nearshore. *Renewable Energy*, 35(6):1516–1527, 2010.

[54] C Guedes Soares, J Bhattacharjee, M Tello, L Pietra, et al. Review and classification of wave energy converters. In *Maritime engineering and technology*, pages 585–594. Taylor & Francis Group London, UK, 2012.

[55] Masami Suzuki and Chuichi Arakawa. Numerical methods to predict characteristics of oscillating water column for terminator type of wave energy converter. In *ISOPE International Ocean and Polar Engineering Conference*, pages ISOPE–I. ISOPE, 2003.

[56] Irina Temiz, Chisom Ekweoba, Sarah Thomas, Morten Kramer, and Andrej Savin. Wave absorber ballast optimization based on the analytical model for a pitching wave energy converter. *Ocean Engineering*, 240:109906, 2021.

[57] T. W. Thorpe. An overview of wave energy technologies. *IEE Colloquium (Digest)*, 1992(110):1–8, 1992.

[58] Tom W Thorpe et al. *A brief review of wave energy*. Harwell Laboratory, Energy Technology Support Unit London, 1999.

[59] Md Imran Uddin and Md Mashud Karim. Application of volume of fluid (vof) method for prediction of wave generated by flow around cambered hydrofoil. *Procedia engineering*, 194:82–89, 2017.

[60] Simon Watson, Alberto Moro, Vera Reis, Charalampos Baniotopoulos, Stephan Barth, Gianni Bartoli, Florian Bauer, Elisa Boelman, Dennis Bosse, Antonello Cherubini, et al. Future emerging technologies in the wind power sector: A european perspective. *Renewable and sustainable energy reviews*, 113:109270, 2019.

[61] Trevor Whittaker and Matt Folley. Nearshore oscillating wave surge converters and the development of oyster. *Philosophical Transactions of*

the Royal Society A: Mathematical, Physical and Engineering Sciences, 370(1959):345–364, 2012.

[62] Michael Yusov, Jack Thwaites, Adi Kurniawan, Jana Orszaghova, and Hugh Wolgamot. New cost-effectiveness metric for wave energy converters-extensive database and comparison. In *Proceedings of the 14th European Wave and Tidal Energy Conference (EWTEC)*, 2021.

[63] Yongxing Zhang, Yongjie Zhao, Wei Sun, and Jiaxuan Li. Ocean wave energy converters: Technical principle, device realization, and performance evaluation. *Renewable and Sustainable Energy Reviews*, 141:110764, 2021.

[64] Siming Zheng. Attenuator wave energy converters. In *Modelling and Optimization of Wave Energy Converters*, pages 201–232. CRC Press, 2022.

[65] Siming Zheng, Alessandro Antonini, Yongliang Zhang, Jon Miles, Deborah Greaves, Guixun Zhu, and Gregorio Iglesias. Hydrodynamic performance of a multi-oscillating water column (owc) platform. *Applied Ocean Research*, 99:102168, 2020.

Acta Universitatis Upsaliensis

Digital Comprehensive Summaries of Uppsala Dissertations from the Faculty of Science and Technology 2500

Editor: The Dean of the Faculty of Science and Technology

A doctoral dissertation from the Faculty of Science and Technology, Uppsala University, is usually a summary of a number of papers. A few copies of the complete dissertation are kept at major Swedish research libraries, while the summary alone is distributed internationally through the series Digital Comprehensive Summaries of Uppsala Dissertations from the Faculty of Science and Technology. (Prior to January, 2005, the series was published under the title "Comprehensive Summaries of Uppsala Dissertations from the Faculty of Science and Technology".)

Distribution: publications.uu.se
urn:nbn:se:uu:diva-548487

ACTA UNIVERSITATIS
UPSALIENSIS
2025